Small-Signal Stability Limits in Inverter-Dominated AC Grids

Master Thesis

Konstantinos Zagkos

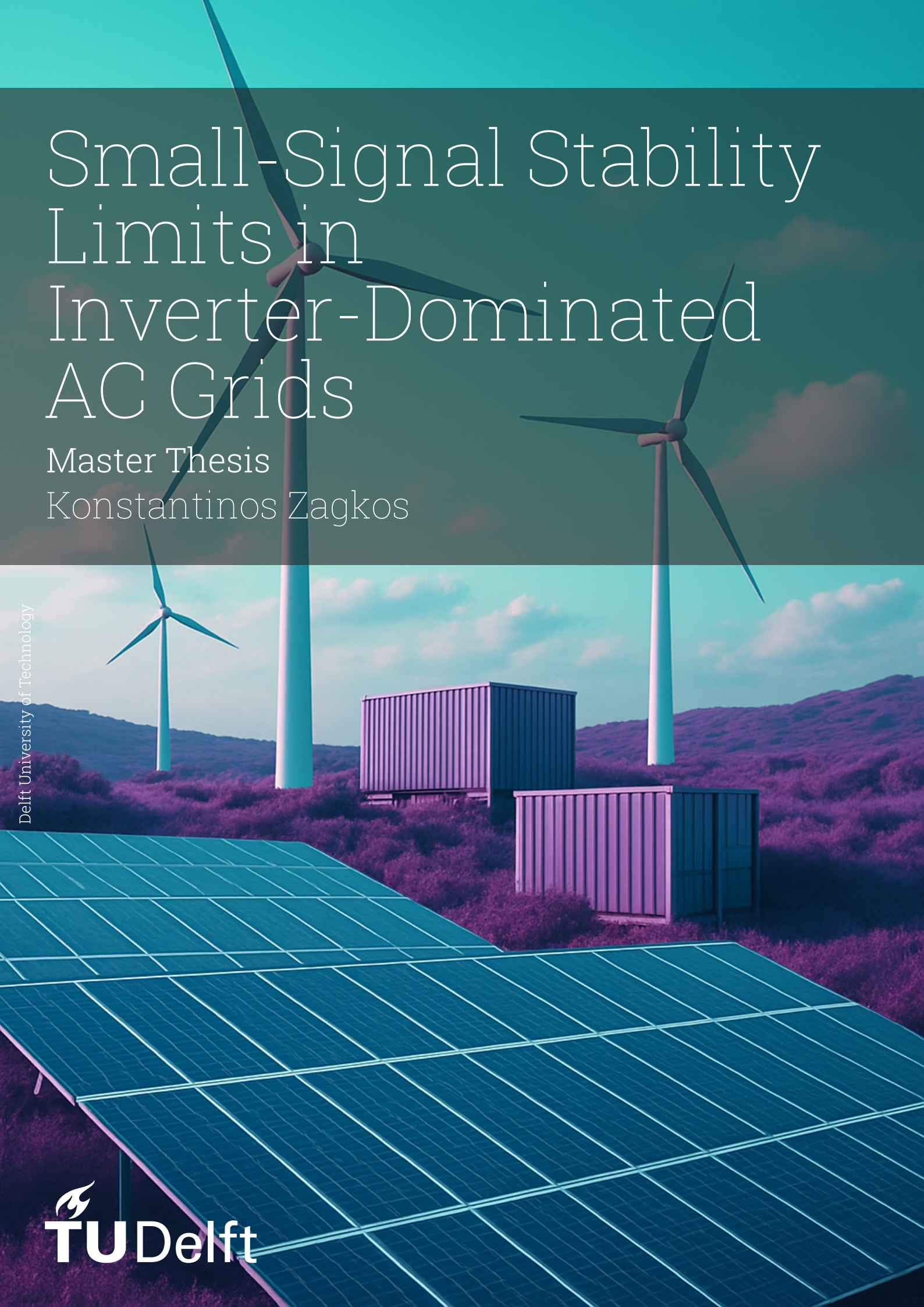

Delft University of Technology

TU Delft

Small-Signal Stability Limits in Inverter-Dominated AC Grids

by

Konstantinos Zagkos

Instructor:	Prof.dr.ir. P. Bauer
Daily Supervisor:	René van Wesenbeeck - Alfen
Project Duration:	December, 2024 - September, 2025
Faculty:	Faculty of Electrical Engineering, Mathematics and Computer Science, Delft

Cover:	Generated by Sora
Style:	TU Delft Report Style, with modifications by Daan Zwaneveld

TU Delft

Preface

I would like to thank my main thesis supervisor, Prof. dr. ir. Pavol Bauer, for the opportunity to work under his guidance. I also thank René van Wesenbeeck and Alfen for the opportunity to work with them and contribute to their research and projects. I am especially grateful for the kind and voluntary help of PhD candidate Tayebeh Faghihisenejani, who, although not my official daily supervisor, supported me greatly towards the end of this project. I would like to thank the committee members, Dr. Jose Rueda-Torres and Dr. Sebastian Rivera Iunnissi, for agreeing to participate and for providing critical feedback on this work. Finally, I thank my family for supporting these studies both financially and mentally, my friends for their constant understanding and guidance, and my TU Delft colleagues, with whom I have spent every day working on our projects and motivating one another.

Konstantinos Zagkos
Delft, September 2025

Summary

This thesis investigates stability limits in inverter-dominated AC grids and how GFM converters can mitigate weaknesses introduced by GFL control. Building on small-signal and impedance-based frameworks, the work first develops dq-admittance models for GFL and GFM inverters and a closed-loop formulation that couples converter and network dynamics. Using graph-theoretic network modelling (grounded Laplacian and Kron reduction), the study integrates generalised short-circuit ratio (gSCR) as a strength metric for multi-infeed systems.

Four case studies validate the framework: a single GFL on an infinite bus, a single GFM, a parallel GFL–GFM pair, and a multi-IBR network. For the single-converter cases, eigenvalue analysis shows the PLL-synchronisation vulnerability of GFL units under weak grids and the instabilities induced in GFM inverters under string grids, proving their duality. The voltage-source behaviour of GFMs is then utilised and used to estimate the minimum GFM penetration needed to stabilise GFLs in weak grid conditions. In multi-IBR settings, gSCR extends SCR to characterise the strength of the whole network. Combined with GFM impedance modelling, it guides the placement of GFM inverters to increase system strength.

The thesis proposes a practical workflow for improving stability in weak multi-IBR networks: identify the critical SCR of representative GFLs via small-signal analysis; compute bus-wise gSCR on the reduced network; assess margins using local single-IBR loop checks; and, by modelling GFMs as voltage sources behind frequency-dependent impedances, select locations/capacities that maximise strength at critical buses. Results show that (i) there exists a critical strength threshold for GFL stability, and adding GFMs raises the effective strength in line with the GFL–GFM duality; (ii) the voltage-source-plus-impedance model predicts how much strengthening GFMs provide; and (iii) while these tools give reliable stability indications, component limits (voltage/current) can still be violated under severe weakness and must be verified in time-domain simulations.

Contents

Nomenclature

Abbreviations

Abbreviation	Definition
IBR	Inverter Based Resource
SCR	Short Circuit Ratio
gSCR	Generalised Short Circuit Ratio
CSCR	Critical Short Circuit Ratio
GFL	Grid Following
GFM	Grid Forming
PCC	Point of Common Coupling
RoCoF	Rate of Change of Frequency
DC	Direct Current
AC	Alternating Current
BESS	Battery Energy Storage System
PV	Photovoltaic
PLL	Phase-Lock Loop
PI	Proportional-integral controller
LCL	Converter-side filter (inductor–capacitor–inductor)

Symbols

Symbol	Definition	Unit
P	Active power	[W]
Q	Reactive power	[Var]
S	Apparent power	[VA]
V_{abc}	Three-phase voltage at PCC	[V]
$I_{C,abc}$	Converter-side three-phase current	[A]
I_{abc}	Three-phase current injected into the AC grid	[A]
U_{abc}	AC grid voltage	[V]
U^*_{abc}	Converter output voltage (from modulation)	[V]
u_{dq}	Direct and quadrature axis voltages in dq-frame	[V]
i_{dq}	Direct and quadrature axis current in dq-frame	[A]
V_{xy}	Direct and quadrature axis voltages in xy- global frame	[V]
I_{xy}	Direct and quadrature axis current in xy- global frame	[A]
K_P	Propotional controler gain	–
K_P	Integrator controler gain	–
J	Virtual Inertia coefficient	$[MVAs^2/rad]$
D	Virtual Damping coefficient	$[MVAs/rad]$
ω	Angular frequency	[rad/s]
θ	Phase angle	[rad]
$\Delta\omega$	Frequency deviation	[rad/s]

1

Introduction

In 2023, electricity generation from wind increased by 10% compared to 2022 [1], while solar power experienced a record growth of 25% and is projected to become the leading energy source by 2029 [2]. These trends align with global efforts to achieve net-zero emissions by 2050. In addition to these renewable sources, battery energy storage systems (BESS) and fuel cells are key technologies that can enhance the utilization of renewable energy. These devices interface with the grid through power electronic inverters. Such inverter-based resources (IBRs) [3], which are expected to dominate future power systems, bring several technical challenges. Besides their dependence on weather conditions and limited dispatchability, IBRs introduce issues such as harmonics, reverse power flow, and reduced system inertia [4]. As the penetration of IBRs increases and conventional synchronous generators (SGs) are phased out, the resulting decline in system inertia and damping has become a major concern for grid stability. Ensuring that future power systems remain stable and resilient is not only a technical challenge but also a cornerstone of energy security and the global transition to a sustainable future.

In traditional power systems, SGs are equipped with inherent inertia, which contributes to system stability. The rotating mass of the generator naturally resists changes in system frequency by absorbing or releasing stored kinetic energy during disturbances. As a result, SGs provide an immediate response to frequency deviations, helping to slow down the changes and giving more time for active control systems to respond [5] [6]. However, as power systems transition towards inverter-based resources (IBRs), which lack physical rotating mass, this natural inertia is being displaced.

Apart from low inertia, another critical challenge associated with the large-scale integration of renewable energy sources is the reduction in system strength [4]. System strength is most commonly defined as the sensitivity of voltage to changes in current injections. In essence, it reflects the voltage stiffness of the grid, playing a role analogous to that of inertia in resisting frequency deviations [7]. System strength is typically characterised by the equivalent grid impedance: high impedance indicates a weak grid, while low impedance indicates a strong one [4]. Several metrics are used to assess system strength, with the Short Circuit Ratio (SCR) being the most widely accepted [8].

The control schemes of IBRs are generally classified into two main categories: Grid-Following (GFL) and Grid-Forming (GFM) inverters. GFL inverters are currently the most widely deployed worldwide. They regulate the inverter's injected current and rely on phase-locked loops (PLLs) to passively track the grid frequency [9]. In contrast, GFM inverters control the output voltage and actively establish the grid voltage and frequency reference [3]. A fundamental duality exists between these two types: GFL inverters tend to face stability challenges under weak grid conditions, whereas GFM inverters may exhibit reduced stability when connected to strong grids [3].

A central question in the ongoing research on inverter-based power systems is: *"How many grid-forming (GFM) inverters are needed to ensure system stability?"* Several studies attempt to answer this by conducting simulations that explore different ratios of grid-following (GFL) and GFM inverters [10]. These works often also consider the impact of inverter placement on overall system stability. In addition to

simulation-based studies, analytical approaches based on small-signal stability analysis are employed to derive more general insights.

In the literature, two primary methods are used to assess system stability. The first is based on impedance models, as developed in [9], [11]–[13], which provide valuable frequency-domain insights. The second relies on state-space models, such as those used in [14] and [15], offering a time-domain perspective. Many of these studies focus on identifying the optimal penetration level of GFM inverters, typically within systems that include both GFL and GFM capacities connected in parallel. However, most existing literature neglects the potential limitations associated with high levels of GFM integration.

This graduation project aims to contribute to this line of research by addressing the question: *"How can operators assess the stability boundaries of networks with high penetration of IBRs?"* To answer this overarching question, the following subquestions will be investigated:

1. What are the stability issues posed by the introduction of GFL IBRs under weak grid conditions?
2. What are the stability issues posed by the introduction of GFM IBRs under strong grid conditions?
3. What mathematical tools can be used to determine the stability boundaries of GFL or GFM IBRs in single inverter systems?
4. What mathematical tools can be used to determine the stability boundaries of GFL or GFM IBRs in a multiple-inverter system?

Among the various metrics available to quantify grid strength, the SCR is the most widely used due to its simplicity and practical applicability. For multi-inverter systems, the generalised SCR (gSCR) provides an effective extension. In this project, impedance-based modelling is preferred over state-space, as it can also be applied in cases where the system parameters are unknown (black box), while it offers significant frequency domain insights.

The structure of this thesis is as follows. In chapter 2, the theoretical background is introduced, including the definition of stability in modern grids, the duality between GFM and GFL converters, and a literature review. Chapter 3 presents the analytical framework, methodology, and tools for assessing the small-signal stability of IBRs. In chapter 4, the stability of different scenarios is examined, starting from single GFL and GFM cases to multi-IBR networks, followed by a discussion of the results. Finally, chapter 5 summarises the main findings and outlines directions for future work.

2

Theoretical Background and Literature Review

This chapter presents the theoretical background and discusses the literature around the stability assessment of inverter-dominated grids. Section 2.1 revisits the classic power-system stability framework and its recent extensions for converter-rich systems. Section 2.2 introduces system strength and the SCR concept. Section 2.3 summarises inverter power-control fundamentals, while Sections 2.4-2.5 characterise the behaviour of GFL and GFM inverters. Section 2.6 frames their duality, followed in section 2.7 by a review of representative GFM schemes (droop, PSC, VSG). Section 2.8 discusses relevant work in the literature. Section 2.9 contrasts state-space and impedance-based modelling as analysis tools. Section 2.10 discusses the system strength indices used later in this thesis, and section 2.11 closes with key takeaways that link to the methodology and case studies.

2.1. Power Grid Stability Classification

2.1.1. Classic Power System Stability Framework

Power system stability, as defined traditionally in 2024 by Prabha Kundrur, is the ability of the system, for a given initial condition, to regain a state of operating equilibrium after being subjected to a physical disturbance, with most system variables bounded so that practically the entire system remains intact [16]. This is the classic IEEE/CIGRE framework, which organises the system dynamics into three main dimensions: the dominant states, the timescale and the disturbance level. While the time scale can be short-term (seconds) and long-term (minutes) and the level of disturbance small or large, the dominant states are the rotor angle, voltage and frequency. These three make the first three stability definitions of the classic framework [17]. These can be seen in figure 2.1.

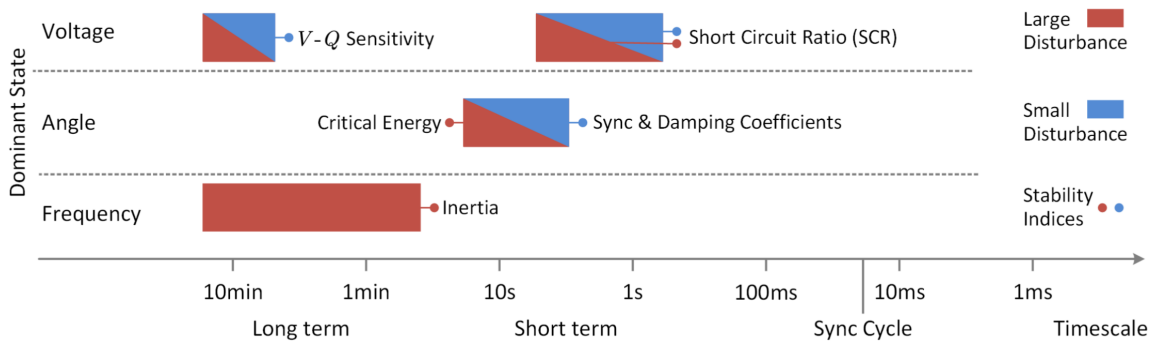

Figure 2.1: Classic stability framework of power systems defined by the IEEE/CIGRE in 2004 [18].

Rotor angle stability is defined as the ability of the interconnected synchronous machines to remain in synchronisation under normal operating conditions and to achieve it again after a disturbance. A machine keeps synchronism if the electromagnetic torque is equal and opposite to the mechanical torque provided. A loss of synchronisation can lead to small-disturbance angle stability, and its indices are the sync and damping coefficients. **Voltage stability** is the ability of a power system to maintain steady voltages close to the nominal value at all buses after a disturbance [17]. Short-term voltage stability is linked with the grid strength and the Short Circuit Ratio (SCR) and long-term with the voltage sensitivity to reactive power ($\partial V/\partial Q$) [18]. Finally, **frequency stability** is the ability to maintain a steady system frequency following a severe imbalance of generation and load. The index for this type of stability is the inertia [18]. The inertia of a power network is defined as the total kinetic energy stored in the rotating masses of the synchronous generators over the system's rated power as seen in equation 2.1 [6].

$$H_{\text{sys}} = \frac{\textit{Total Kinetic Energy Stored}}{\textit{System Rated Power}} = \frac{\sum_i \left(\frac{1}{2} J\omega^2\right)_i}{S_{\text{sys}}} \tag{2.1}$$

where J is the moment of inertia of the machine i, and ω is the angular synchronous frequency.

2.1.2. Extension of the classic framework

All these definitions were established in 2004, when power grids were still dominated by synchronous generators. However, modern grids are increasingly populated by IBRs which, despite their many benefits, introduce a range of new challenges. The main stability issues arise from the interaction of IBR control systems, the overall reduction in system inertia, and their limited contribution to short-circuit currents during faults. In response, the classical framework was revisited by Hatziargyriou in 2021 [17], who introduced two additional stability categories. The first, **resonance stability**, refers to oscillations that occur when inverter control loops, filters, or network elements interact with grid impedances, often manifesting as sub- or supersynchronous resonances and resulting in poorly damped or unstable modes. The second, **converter-driven stability**, describes instabilities originating from the fast control loops and algorithms of IBRs, such as inner current controllers and PLLs. Because these controllers operate at timescales that can couple with both machine dynamics and network transients, they may induce system-wide instability.

Building upon on that, in 2023, Gu and Green extended this categorisation even further. The previously called converter-driven stability is now part of the Electromagnetic (EM) stability, which covers sub- and supersynchronous resonances excited by inverter control and filter dynamics, near and above the fundamental frequency. EM stability is a new dominant state added to the framework as shown in figure 2.2. Apart from that, three more characteristics are added to the first three categories and show how the IBRs have influenced them. **Generalized angle stability** broadens the traditional notion of rotor angle stability by including synchronization mechanisms of inverters, such as PLLs and virtual oscillators, whose bandwidths can reach several Hz and overlap with electromechanical modes. **Indirect voltage stability** reflects the fact that many IBRs, especially GFL inverters, regulate voltage only indirectly through reactive power control, which shifts voltage dynamics into the sub-second range and couples them with angle and frequency behavior. Finally, **fast frequency dynamics** capture the reduced inertia and faster active power responses of converter-based resources, which compress frequency phenomena from tens of seconds into seconds [18].

The key takeaway for these two extensions of the classic framework is the overlap of time scales (as shown in figure 2.2 with the arrows). This overlap in timescales (voltage–angle, angle–frequency, EM–angle) poses risks of dynamic interaction and makes the stability analysis more complicated [18].

2.2. System Strength and SCR

As discussed in the previous section, an index of voltage stability is the system strength. Strength is the ability of the grid to withstand most sudden changes in operating conditions. This means that the voltage is within acceptable limits after a disturbance. A simple metric for system strength, commonly used for IBR-dominated grids, is the short-circuit ratio (SCR). We assume a simplified grid, by obtaining the Thevenin equivalent, with an SG connected to the rest of the grid at the point of common coupling (PCC)

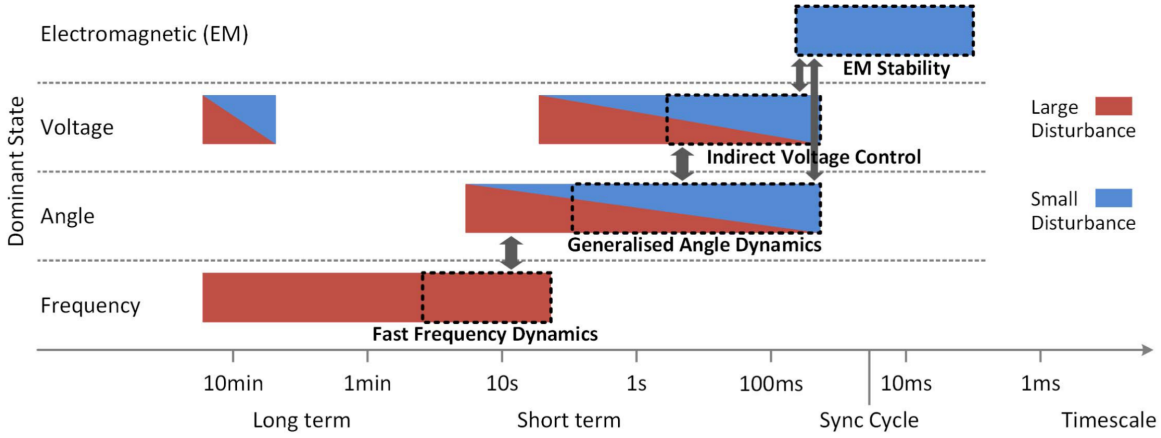

Figure 2.2: New power system stability framework by Gu and Green [18].

through an equivalent impedance of the network Z_{Th} as seen in figure 2.3. If the short circuit occurs at the PCC, the SG has to deliver the short circuit power to that location, as shown in equation 2.2.

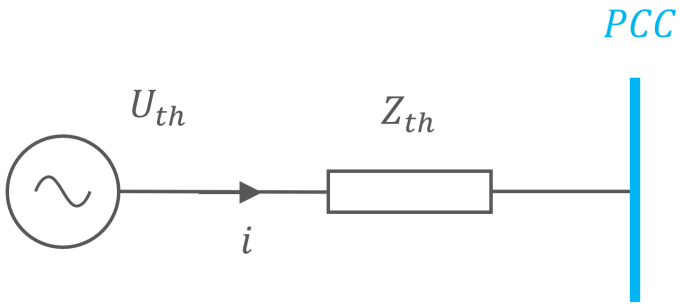

Figure 2.3: Thevenin equivalent circuit of SG connected to the main grid.

$$S_{sc} = \frac{U_{th}^2}{Z_{th}} \tag{2.2}$$

The SCR is considered the ratio of the short circuit power over the rated power of the component to this point:

$$SCR = \frac{S_{sc}}{S_{rated}} = \frac{U_{th}^2}{Z_{th} S_{rated}} = \frac{Z_{base}}{Z_{th}} = \frac{1}{Z_{th,pu}} \tag{2.3}$$

where P_{rated} is the rated power of the generator and U_{th} and Z_{th} are base values.

High SCR (small Thevenin impedance) indicates a “strong” grid with stiff voltage. Low SCR indicates a “weak” grid where reactive injections and control dynamics strongly affect voltage and are prone to instability.

The IEEE standard 1204-1997 [19] defines the values of SCR that can determine the strength of a grid. For values higher than 3 the grid is considered as strong or stiff, while values of between 2 and 3 indicate a weak grid. Values below 2 indicate a very weak grid. All these values are summarised in table 2.1.

Operating the system in a weak grid (SCR < 3) can lead to several challenges, including frequency resonance, voltage instability and overvoltages caused by load rejections.

SCR value	Grid Strength
$SCR > 3$	Strong
$2 < SCR < 3$	Weak
$SCR < 2$	Very Weak

Table 2.1: Short Circuit Ratio Classification

The problem of the IBRs under weak grid conditions is because of PLLs and the inner-current control loop, which play a major role in the dynamic recovery after a fault. For connection points with low SCR, the response of the inner current-control loop and PLL can become oscillatory. This is due to the PLL having difficulty synchronising with the distorted network voltage, and also due to high gains in the inner-current control loop and PLL. This can be mitigated by reducing the gains of both controllers. The exact value of the SCR at which the instability may occur depends on the inverter vendor and network configuration. A typical range of SCRs below which this may occur is 1.5 to 2 [17]. This value, where the instability occurs, is also mentioned in the literature as critical SCR (CSCR) [11].

2.3. Inverter Power Control

Inverters are essential devices that convert direct current (DC) into alternating current (AC) enabling the integration of various power sources into AC power systems, by injecting active and reactive power. DC sources like photovoltaic (PV) or BESS need to convert their DC power generated to AC. However, most common technologies include DC-DC converters connected in series with an inverter, in order to increase the controllability of the source. The same applies to AC sources as well, such as wind turbines or microturbines, where an AC-DC converter is connected back-to-back with the inverter [20], [21].

Unlike synchronous machines, where mechanical and electrical characteristics define control limits, power converters rely primarily on controller configuration to achieve the desired electrical performance [22]. The principles of inverter power control are formulated based on fundamental active power control. Assume the simple circuit depicted in figure 2.4. This figure includes a power source, interfaced through an inverter, connected to the PCC through an impedance. For the High Voltage (HV) and Medium voltage (MV) grids the transmission lines are primarily inductive. In contrast, in the Low Voltage (LV) grids, the resistive component is higher. In this case, an inductive grid is assumed.

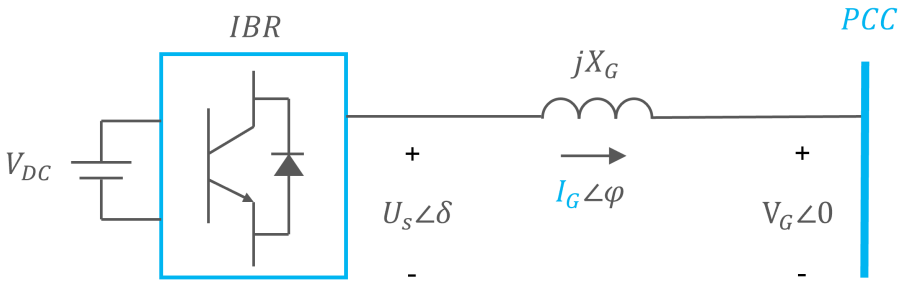

Figure 2.4: Inverter-based resource connected to the main grid.

$$P = \frac{U_S V_G \sin\delta}{X_G}$$
$$Q = \frac{U_S^2 - U_S V_G \cos\delta}{X_G} \tag{2.4}$$

From equation 2.4, it can be seen that the power injected into the grid can be controlled through the current I_g or the source voltage U_s when the grid voltage V_g is considered constant. Based on the selection of either current or voltage, the inverters can be classified into Grid-Following (GFL) and Grid-Forming (GFM), respectively.

2.4. Grid Following (GFL) Inverters

Grid-following (GFL) power converters are grid-connected converters that inject current into the grid. Thus, they operate as controllable current sources to deliver the desired active and reactive power to the grid. This can be seen on the simplified diagram of the converter in figure 2.5 [20]. The current source is in parallel with a big impedance, to show that the source is not disturbing the voltage of the grid and that it can operate with other parallel current sources without conflicting. The P^* and Q^* are the active and reactive power set points to be delivered to the grid. To achieve this, the controller needs to synchronise (follow) with the grid voltage in terms of amplitude, frequency, and phase angle. That is achieved via a Phase-Locked Loop (PLL).

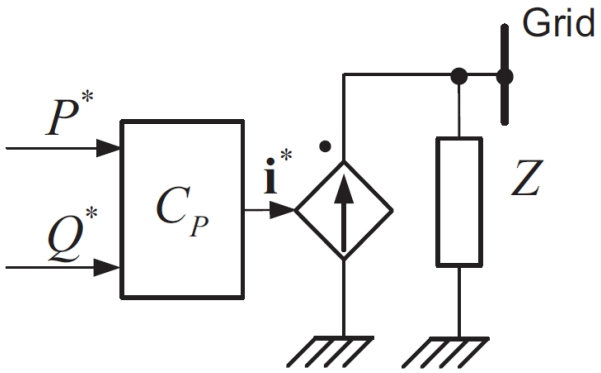

Figure 2.5: Simplified diagram of GFL power converter [20].

In three-phase systems, the synchronous-reference-frame phase-locked loop (SRF-PLL) is commonly used as the synchronisation technique with the grid. The structure of the SRF-PLL is shown in figure 2.6. The instantaneous voltage at the PCC is measured and then translated from the abc reference frame to the dq frame. The PLL aims to align the a-axis of the three-phase system with either the d- or the q-axis of the rotating frame [23]. In the figure, the phase is aligned with the d-axis and the q-axis is forced to zero. This generates an estimate of the frequency, where the nominal frequency ω^* is added as a feedforward term to improve the dynamics of the phase estimation θ' [20].

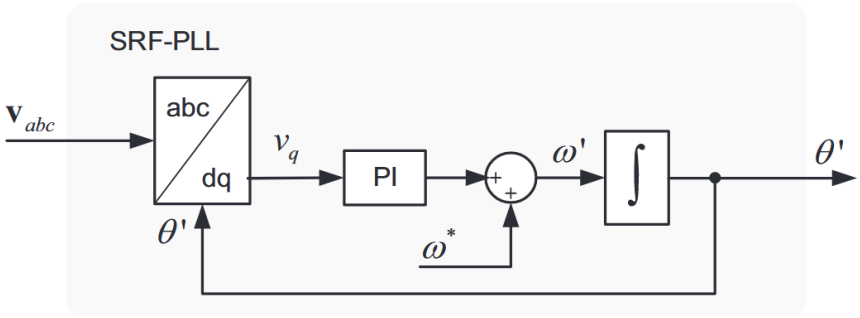

Figure 2.6: Structure of the synchronous reference frame phase-locked loop [20].

Apart from the synchronisation loop, the typical GFL control includes vector current control that regulates the injected currents. The current references are generated by outer power-control loops directly from the reference values P^* and Q^* [20]. The current references can also be set indirectly by implementing direct voltage control (DVC) or alternating voltage control (AVC), by regulating the DC-link voltage on the DC side of the inverter or the AC voltage at the grid side, respectively. Usually,

proportional–integral (PI) controllers are utilised, with the addition of a voltage feedforward term for improved dynamic response [24].

2.5. Grid Forming (GFM) Inverters

Grid Forming (GFM) power converters are grid-connected converters that supply their reactive power by controlling the source voltage U_s and the power angle δ as seen in equation 2.4 [22]. The simplified equivalent circuit of a GFM converter is illustrated in figure 2.7. As seen from the figure they behave as controllable voltage sources in series with a low impedance. This impedance complicates its operation when running in parallel with other GFM converters, meaning that their physical output impedances primarily influence the natural current sharing among converters [20]. The goal of GFM controllers is to maintain a stable PCC voltage at the reference value $V_{PCC} = V^*$ and frequency ω^* [20]. These two references can be generated by the reactive and active power control (RPC and APC), respectively [24].

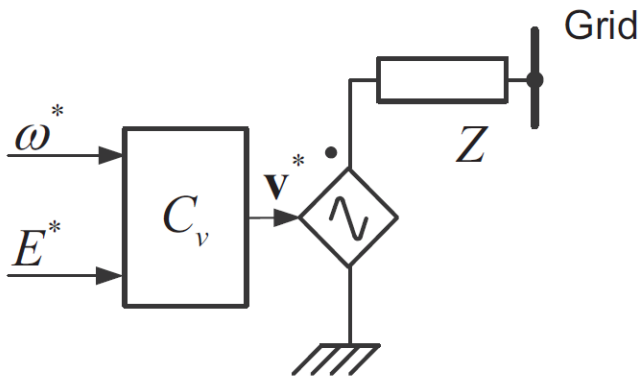

Figure 2.7: Simplified diagram of GFM power converter [20].

There are many different APC and RPC schemes, with the most famous to be the droop control, the power synchronization control (PSC) and the virtual synchronous generator (VSG) control. These three methods are described later in the report. The synchronisation with the grid is achieved by the APC while RPC generates the voltage reference. These references are fed to the inner voltage control loop is used to regulate the output voltage of the inverter, which is further cascaded with the current control loop for the overcurrent limitation [24].

2.6. Duality of GFL and GFM control

Both GFL and GFM control are used for grid-connected inverters but they have different operations due to their different inherent characteristics. GFL control behaves as a current source that injects the needed power into the grid. Since they use PLLs to operate they require a stiff and stable voltage at the terminal. On the other hand, GFM inverters, by definition should be able to set up a stable grid voltage and frequency under normal, islanded, blackout and restoration states without relying on SGs [20].

Assume a change in the grid voltage (PCC). the GFL response can be seen in figure 2.8. Since the inverter is injecting constant current, the voltage of the source E_s has to be adjusted in response to the new grid voltage which might lead to voltage violations, before synchronization occurs to restore I_g to follow V_g. On the other hand, on figure 2.9 the response of a GFM inverter is presented. When there is a change in voltage, the GFM keeps the source voltage E_s stable and it adjusts the current and subsequently the power angle δ. However, this behaviour during fault conditions might lead to high-fault currents that might affect the solid-state devices of the inverters. Therefore, current limiting mechanisms are needed [22].

Apart from the differences between GFL and GFM inverters, the literature has also revealed a duality in the relationship between the two types. Firstly, this can be understood from their grid-interfacing

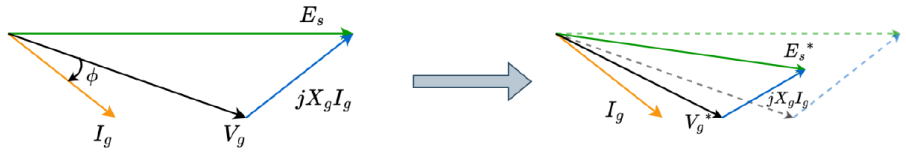

Figure 2.8: Phasor diagram of performance of GFL controller after disturbance [22].

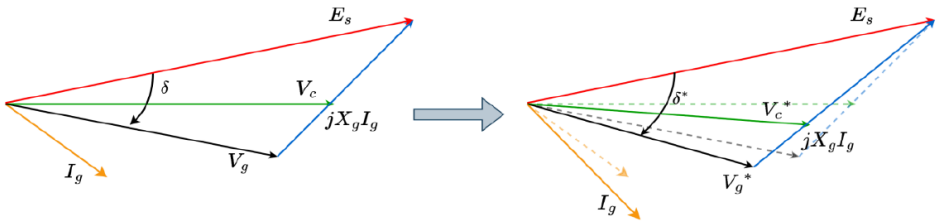

Figure 2.9: Phasor diagram of performance of GFM controller after disturbance [22].

behaviour. Modern grids are typically considered as voltage sources with loads connected in parallel. This means that a GFL inverter is *voltage-following*, since the PLL tracks the grid voltage, while a GFM inverter is *voltage-forming*. However, since GFL inverters inject current, they can also be considered *current-forming*. In contrast, GFM inverters with a power-synchronisation loop are regarded as *current-following* [3].

The synchronisation mechanisms of GFM and GFL also show a clear duality. In GFL inverters, synchronisation is achieved through PLL, which tracks the grid angle by regulating the v_q component to zero. In GFM inverters, the internal angle is established instead through active-power vs. frequency ($P\omega$) droop, which adjusts the internal frequency so that power balance enforces phase synchronisation with the grid. These two structures are mathematically dual: the PLL can be seen as a $v_q\omega$ (or $Q\omega$) droop, while the $P\omega$ droop behaves like an $i_d - \omega$ synchroniser. Both have the same function of aligning the inverter's internal reference with the grid [3].

Finally, the swing dynamics also show duality. In GFM, the inverter exhibits a current or active-power versus angle swing, resembling the swing equation of a synchronous machine, where inertia and damping can be emulated through droop filters or virtual synchronous generator control [24]. In GFL, by contrast, the dynamics appear as a voltage or reactive-power versus angle swing, shaped by the PLL loop gains [3].

2.6.1. Duality of System Strength

As discussed before, the grid is mostly viewed as a voltage source in modern grids. System strength in section 2.2 was defined as a voltage stability index. Thus, this strength can be referred to as grid voltage strength. Based on the duality theory, grid current duality is also defined in [3]. Any source can be seen as either a voltage or a current source by using Thevenin's and Norton's theorems. A voltage source is close to an ideal voltage source when it is in series with a small impedance Z_g. The smaller the Z_g, the stronger (or stiffer) the voltage source. As a dual, a current source is close to an ideal current source when the parallel impedance Y_g is small. The smaller the Y_g, the stronger (or stiffer) the current source. This concept is illustrated in figure 2.10.

As discussed before, GFL inverters (voltage-following, current-forming) are vulnerable to weak-voltage grids (or strong-current grids) and cannot operate under open-circuit conditions. Intuitively, this means that the GFL does not have a strong grid to follow and cannot inject current. GFM inverters (current-following, voltage-forming) are vulnerable to weak-current grids (or strong-voltage grids) and cannot operate under short-circuit conditions. Intuitively, this means that the GFM cannot impose its voltage since the grid is already too stiff [3].

All above observations are summarised in table 2.2.

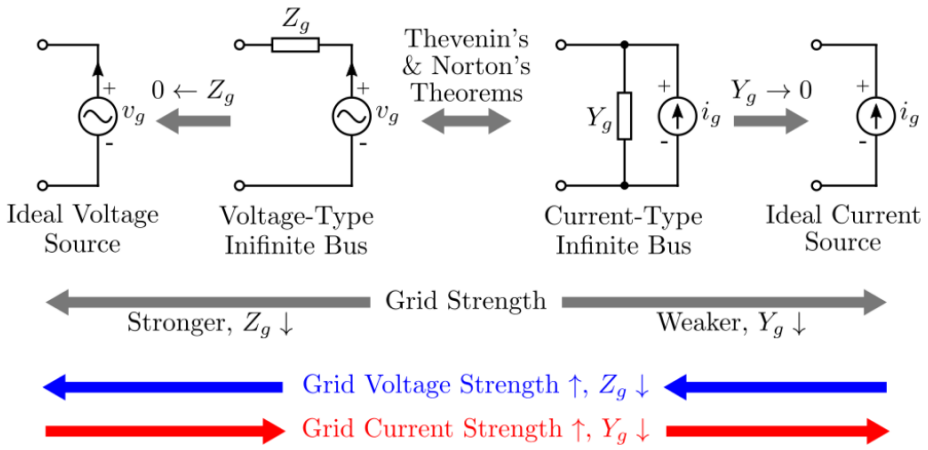

Figure 2.10: Duality of grid strength [3].

2.7. Grid Forming Control Schemes

In this section, the different synchronisation approaches used in GFM control are presented. Generally, the GFM control structure consists of inner control loops for current and outer loops for voltage. A current-limiting scheme can be implemented between the voltage and current control loops to prevent current overloads and ensure that solid-state devices operate within acceptable limits [22]. As mentioned in section 2.5 GFM control does not support power-sharing control among parallel converters. To address this limitation, many strategies have been proposed in the literature that require the inverters interconnected via high-bandwidth communication networks [20]. In the scope of this project, the focus is on local controllers that can achieve power sharing without the need for communication links, which enhances reliability while reducing technical complexity and costs.

2.7.1. Droop Control

In the general case, the active and reactive power that can be delivered to the PCC is shown in equation 2.5.

$$\begin{aligned} P &= \frac{U_s}{R^2 + X_g^2} \left[R(U_s - V_g \cos\delta) + X_g V_g \sin\delta \right], \\ Q &= \frac{U_s}{R^2 + X_g^2} \left[-RV_g \sin\delta + X_g(U_s - V_g \cos\delta) \right]. \end{aligned} \tag{2.5}$$

In the HV and MV cases where $X >> R$ the delivered power is equal to equation 2.6. A small power angle δ is assumed. Therefore $sin\delta \approx \delta$ and $cos\delta \approx 1$.

$$\begin{aligned} P_A &\approx \frac{U_s}{X_g} (V_g \sin\delta) \quad \Rightarrow \quad \delta \approx \frac{X_g P_A}{U_s V_g}, \\ Q_A &\approx \frac{U_s}{X_g} (U_s - V_g \cos\delta) \quad \Rightarrow \quad U_s - V_g \approx \frac{X_g Q_A}{U_s}. \end{aligned} \tag{2.6}$$

The equation 2.6 shows that active and reactive power flows can be controlled independently. The active power flow is primarily influenced by the phase difference between source and grid voltages, while the reactive power flow is determined by the difference in voltage amplitude. Therefore the main principle of droop control is the active power control (APC) and the reactive power control (RPC) laws as presented in equation 2.7.

$$\begin{aligned} f &= f_0 - k_P(P - P_{\text{set}}) \\ V &= V_0 - k_Q(Q - Q_{\text{set}}) \end{aligned} \tag{2.7}$$

Table 2.2: Comparison of GFL and GFM inverters based on their characteristics and duality.

Characteristic	GFL (Grid-Following)	GFM (Grid-Forming)
Grid interfacing	Voltage-following, current-forming. Injects controlled currents into the grid. Requires a stiff voltage source to operate.	Voltage-forming, current-following. Imposes terminal voltage and lets current adjust according to network conditions.
Synchronization mechanism	Phase-locked loop (PLL), aligns d-axis by driving $v_q \to 0$. Requires an external voltage reference.	P–ω droop (or variants, e.g. VSG, PSC). Internal angle set by power balance.
Swing dynamics	Voltage/reactive-power vs. angle swing. Shaped by PLL loop gains.	Current/active-power vs. angle swing. Resembles synchronous machine swing equation with inertia and damping emulation.
Grid strength dependency	Vulnerable to weak-voltage grids (high Z_g, low SCR). Cannot operate under open-circuit conditions.	Vulnerable to strong-voltage grids (low Z_g, stiff system). Cannot operate under short-circuit conditions.
Operation scenarios	Suitable for strong and stable grids. Cannot form voltage in islanded or blackout conditions.	Can establish voltage and frequency in islanded, blackout, and restoration states. Requires current-limiting protections under faults.

where f_0 the nominal frequency, V_0 the nominal voltage, k_P and k_Q the droop coefficients, which actually define the slope of the droop characteristics as seen in figure 2.11. The power angle δ and the frequency are proportional as seen in equation 2.8.

$$\frac{d\delta}{dt} = 2\pi(f - f_{\text{grid}}) = \omega - \omega_{grid} \tag{2.8}$$

These two relationships show that the frequency and the voltage of the grid can be regulated by adjusting the active and reactive power delivered to the grid. When the frequency is lower than the nominal f_0, the inverter has to offer more power to the grid, and vice versa. The same applies to voltage. In a voltage sag the inverter has to offer more reactive power to bring the voltage back to nominal levels.

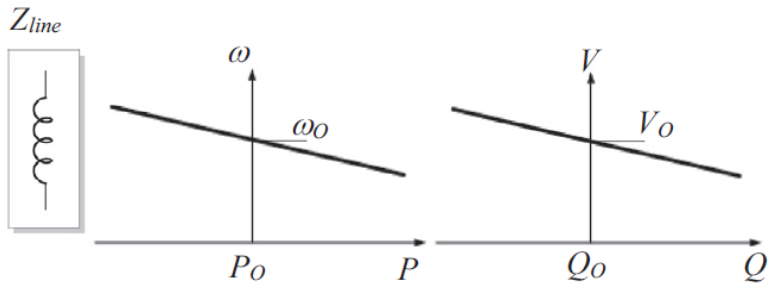

Figure 2.11: Frequency and voltage droop characteristics in grids with dominant inductive behavior

Based on equation 2.7 the references for the frequency and voltage can be calculated before entering the voltage and current loops. In the dq frame, V_q is assumed to be zero and the droop control can be implemented on the d axis.

2.7.2. Power Synchronization Control (PSC)

The Power Synchronization Control (PSC) is a method for controlling grid-connected voltage-source converters (VSCs) that mimics the synchronization mechanism of synchronous machines in AC systems. In a system with a generator and a motor, an increase in the generator's torque causes its

electromotive force (EMF) to advance in phase. This phase shift creates a difference between the EMFs of the two machines, which translates into power transfer from the generator to the motor. As the motor receives more power, its electromagnetic torque increases, leading to a corresponding phase shift in its own EMF. Consequently, the phase difference between the two EMFs gradually decreases until the system reaches a new steady-state equilibrium [25].

PSC directly utilizes the power-transfer dynamics between the VSC and AC systems. The PSC inherently maintains synchronization without the need for an external PLL by regulating the power exchange between the converter and the grid.

The PSC control law is shown in equation 2.9.

$$\frac{d\Delta\delta}{dt} = k_p(P_{\text{ref}} - P) \tag{2.9}$$

where δ is the power angle, k_p is the controller gain, P_{ref} is the active power setpoint and P is the actual measured active power.

In this control scheme, the power angle of the VSC output voltage is adjusted to regulate active power flow, inherently ensuring synchronization between the VSC and the grid. The transmitted power is increased or decreased by shifting the output voltage phasor of the VSC forwards or backwards. In PSC the need for an inner current control loop is not necessary. The reactive power is controlled by the voltage magnitude, similar to droop control.

This approach enhances stability, particularly in weak AC system connections, and enables the VSC to provide voltage support similar to that of a synchronous machine.

2.7.3. Virtual Synchronous Generator (VSG) Control

To address the challenge of low inertia in systems with a high penetration of inverter-based resources, one solution is to emulate a synchronous generator by implementing control algorithms that replicate the functions of excitation, governor, and rotor dynamics. A fundamental approach to this is the Virtual Synchronous Generator (VSG), which enhances system stability by providing angular frequency support.

The VSG emulates the rotor dynamics (the rotor swing equation) as well as the governor dynamics of an SG. The rotor swing equation includes damping and inertia coefficients and is implemented to determine the reference for the angular speed (and angle), as seen in equation 2.10.

$$P_{\text{set}} - P = J\omega_0 \frac{d\omega}{dt} + D(\omega - \omega_0) \tag{2.10}$$

where ω is the angular frequency, ω_0 the nominal frequency, J the inertia constant, D the damping coefficient, P the actual power supplied by the inverter and P_set the setpoint for active power.

The governor model dynamics include an active power droop controller as shown in equation 2.11

$$P_{\text{set}} = P_{\text{ref}} + K_p(\omega - \omega_0) \tag{2.11}$$

where P_{ref} is a control variable and K_p is the governor stiffness factor.

The voltage regulation follows a reactive power droop control mechanism, which differs from the conventional approach, as seen in equation 2.12.

$$K_v \frac{dV}{dt} = Q_{\text{set}} - Q - D_q\,(V - V_{\text{ref}}) \tag{2.12}$$

where K_v is the voltage integral gain, Q is the actual reactive power supplied by the inverter, Q_{set} the setpoint for reactive power and D_q is the droop coefficient of the controller.

The completed control diagram of VSG control with the three modules discussed is illustrated in figure 2.12.

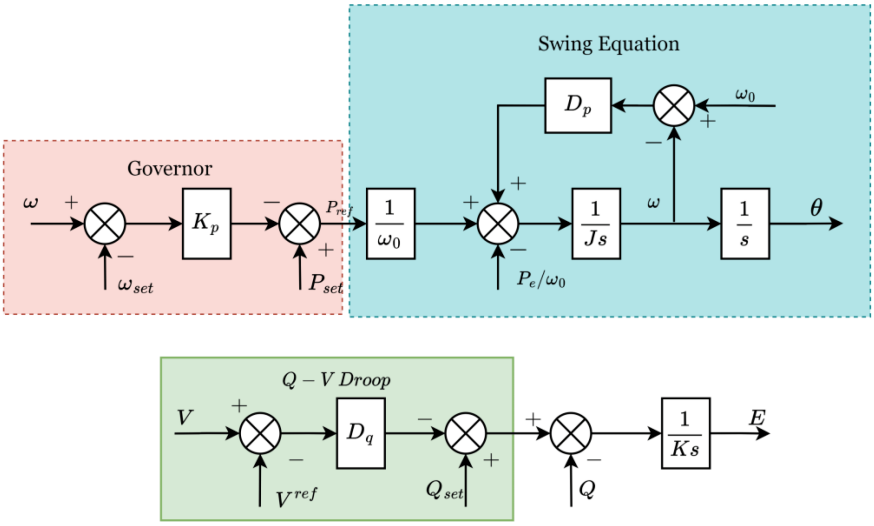

Figure 2.12: Control diagram of virtual synchronous generator control [22].

The VSG is a virtual inertia implementation of conventional droop control. However, it requires energy storage to emulate the stored energy in the rotating masses of SGs. The benefit of this approach lies in the controllability provided by multiple tunable coefficients, which, in the case of physical machines, are dictated by inherent characteristics. The main limitation is that VSGs may experience oscillations when connected to the grid [22].

In addition to the three strategies discussed above, several other synchronisation techniques have been proposed in the literature, such as Matching Control [26], Virtual Oscillator Control (VOC) [27], and Dispatchable VOC [28]. However, these methods fall outside the scope of the present research.

2.8. Literature review

Many researchers have examined stability issues under high penetration of IBRs. The main questions revolve around what level of GFL penetration can cause instabilities and how GFM can mitigate these problems. Several studies address this by simulating different GFL–GFM ratios in test grids, such as Geekiyanage et al. [10], who tested the two-area Kundur system under varying IBR penetrations. They found that when IBR penetration exceeded 75%, the system collapsed. On a larger scale, Liu et al. [29] developed a transmission–distribution co-simulation model with 100% IBR penetration, showing that for IBR shares above 80% the system could not maintain stability, while introducing just 12% GFM improved the frequency response. Although such simulation-based approaches provide useful insights and reveal general trends, their results are case-specific and highly dependent on the test grid and the location of GFM resources.

In an effort to develop a more generalised approach that could be applied to different grids and operators, analytical methods were introduced to test system stability without relying solely on time-domain simulations. Most of these works follow two main approaches: state-space (SS) modelling and impedance/admittance modelling.

Beginning with the first, Ji et al. [14] build full-order state-space models for GFL and VSG-type GFM inverters, aggregate them into a hybrid plant, and study small-signal stability via eigenvalue analysis validated against simulations. Their results show that weak grids (larger L_g) drive GFL poles rightward, while adding one GFM shifts dominant poles leftward and improves damping. However, the findings are case-study specific (three small inverters in parallel connected to a voltage source), and therefore do not translate into universal placement rules or a minimum GFM share. Similarly, Gao et al. [15] develop state-space models for the same types of converters and study eigenvalue trajectories versus SCR. They find that GFLs lose stability in weak grids (SCR $\lesssim 1.58$), while GFMs remain stable under

weak grids but can become unstable for high SCR values (SCR $\gtrsim 11.7$). Theoretical predictions are validated through simulations and laboratory experiments. However, the test case considers only a single converter rather than multiple interconnected ones.

The second approach, impedance-based modeling, provides valuable frequency-domain insights. Starting with Dong et al. [11], this was the first work to introduce the concept of the generalised short-circuit ratio (gSCR) for multi-infeed IBR systems, extending the SCR definition from single-infeed systems. A key insight is that the stability margins of a single GFL can be generalized to larger grids with homogeneous GFLs, enabling stability assessment without full-scale simulations. Building on this, Xin et al. [9] showed that a properly tuned GFM behaves like a stiff voltage source in the low- to mid-frequency band (around the PLL bandwidth). They also addressed the question of "how many GFMs are needed" by employing the gSCR framework and analysing a hybrid system of GFLs operating in parallel with GFMs. While the paper offers strong insights into the stiff-voltage behaviour of GFMs, the assumption of equal GFM/GFL penetration across all IBRs in a grid is not very realistic.

Henderson et al. [12], by combining MIMO impedance-based disk margins with the grid-strength impedance metric (GSIM), define the minimum, optimal, and maximum penetration levels of GFMs in multi-IBR systems. The optimum level provides maximum robustness (rather than strength), while the maximum level corresponds to the upper stability boundary for GFM penetration. In parallel, Yang et al. [30] employed the gSCR framework to rigorously prove that replacing a GFL with a GFM improves the effective grid strength. They further developed an algorithm to determine the optimal placement of GFMs to maximise grid strength, which is a more realistic approach compared to Xin et al. and Ji et al., where GFM capacities are assumed to be connected in parallel to every GFL. The limitation, however, is that GFMs must be treated as ideally stiff voltage sources for the method to hold.

Finally, Liu et al. [31] formulated a system-strength-constrained planning method for GFM-based energy storage systems. Using the gSCR framework and solving a quadratic-support-function optimisation problem, they determined the optimal sizing and placement of GFMs. Similar to the Yang case, the dynamics of GFMs are merged into the network admittance matrix.

2.9. Comparison between state-space and impedance modelling

To analyse the stability of a non-linear system, like the grid-connected GFL and GFM inverters, small signal linearised model is an effective tool. State-space and impedance-based methods are two widely used approaches, as seen in the previous review. Each one has its own advantages and disadvantages [32].

The state-space method is a classical approach for small-signal stability analysis. By linearising the system dynamics and forming the state-space matrix, the eigenvalues can be calculated, and the stability boundary is easy to be found easily as well. This method is accurate for white-box systems, since all parameters of the converter and network can be captured. However, it requires complete knowledge of the converter control design, which is often difficult to know. This limitation makes the state-space approach less suitable when working with realistic or partially known systems [32].

In contrast, the impedance-based method represents each subsystem (converter, grid, or filter) by its small-signal impedance or admittance and then interconnects them to form the closed-loop system. Stability can then be assessed using the generalised Nyquist criterion (GNC). A key advantage is that it does not require knowledge of the details of the whole system. Impedances can be directly measured or identified experimentally (with frequency scan methods), making the method applicable even to black-box systems [32]. Apart from that, the impedance approach provides a clear frequency-domain view of interactions between converters and the grid, which is the main issue of the modern IBR-rich networks, as discussed in section 2.1.

A comparison between these two methods is presented in table 2.3. Although determining the stability boundary is more challenging with impedance methods compared to state-space modelling, impedance remains a more suitable first approach for stability studies of inverters. Its main advantages are the black-box applicability and the clearer visualisation it provides in terms of frequency-domain insights and the interaction of interconnected components. Moreover, since GFL and GFM inverters can be modelled as current sources or voltage sources in parallel or in series with an impedance, choosing

this approach might be useful. Based on this review, impedance modelling is therefore selected as the approach for this work.

Table 2.3: Comparison of state-space and impedance methods [32].

Methods	State-space	Impedance
Applicable range (for white-box system)	Wide	Medium
Availability for black-box system	No	Yes
Visualization	Medium	High
Scalability (for multi-converter system)	High	High
Difficulty about seeking stability margin	Good	Medium

2.10. Power system strength indices

As seen in the literature, the gSCR is the most widely used method to assess power system strength in cases with interconnected IBRs. For single-IBR systems, the classical SCR is sufficient, but researchers have attempted to extend it to larger grids with multiple interconnected IBRs. Before the development of gSCR, several alternative indices were proposed. For example, the weighted SCR and the composite SCR were introduced, but these approaches did not account for the shared impedances of the IBR control loops [33]. To address this, the site-dependent SCR was proposed, which evaluates grid strength in terms of static voltage stability [11], though it has not yet been validated through EMT simulations [33]. The gSCR overcomes these shortcomings. Early versions were based on power-based models, but still neglected the actual electrical network connections. The gSCR presented in Dong et al. [11], however, is derived from impedance models and resolves this issue. Naturally, gSCR also has limitations. For instance, it does not consider shunt capacitors or control devices such as FACTS, a gap addressed by Liyanarachchi et al. [33]. Moreover, gSCR assumes nominal operating conditions. Under non-nominal conditions, the generalised Operational SCR (gOSCR) can be applied [34]. However, these two approaches are tailored to specific cases and do not provide a universal framework.

2.11. Conclusion

Based on the literature review, many approaches have been developed to assess the strength and stability of grids with high IBR penetration. Most of these focus on instabilities associated with GFL control, rather than those from the increasing use of GFM control. This thesis aims to revisit the techniques presented in the literature from a duality theory perspective (see section 2.6), by assessing the instabilities introduced by both GFL and GFM inverters. Apart from that, a combination of gSCR and the ideal voltage source behaviour of the GFM inverters is implemented.

Accordingly, impedance models and the gSCR framework are selected as the methods to evaluate system stability and strength, as they complement each other effectively. The approach is structured as follows: first, single GFL and GFM grid-connected inverters are modelled, and their stability boundaries are determined in relation to system strength (SCR). This analysis is then extended to multi-IBR systems. We begin with grids comprising only GFL inverters, assessing their stability (gSCR), and subsequently introduce GFM inverters to examine how grid strength improves.

3

Modelling and Methods

This chapter develops the modelling framework used in the remainder of the thesis. Section 3.1 shows the closed-loop representation adopted throughout, and section 3.2 derives the grid admittance seen by a single IBR terminal. Sections 3.3-3.4 build the dq admittance models for GFL and GFM converters, and section 3.5 models them as voltage sources behind equivalent impedances. Sections 3.6-3.7 present the power-network modelling, grounded Laplacian, and Kron reduction and integrate the gSCR index to measure strength. Finally, sections 3.8–3.9 present the multi-IBR closed loop system and explain how to perform the stability assessment by decoupling the system.

3.1. System Closed Loop

A typical setup of a single IBR connected to the grid is shown in figure 3.1. The IBR is connected through a filter (LC in this case) and through the line impedance L_g to the infinite bus. The voltage generated by the inverter is U_{abc}. The IBR terminal voltage is considered the point after the filter. This terminal voltage is denoted as V_{abc}. The voltage at the infinite bus is denoted as $Vg_{,abc}$. The current Ic_{abc} flows from the controller to the filter, and I_{abc} from the filter to the grid.

To evaluate the small-signal stability of the system, an impedance-based modelling approach is employed. This involves linearizing the nonlinear model that describes the relationships between voltages and currents. The linearization is performed using a first-order Taylor expansion around a steady-state operating point (x_0). Using perturbation theory, each variable is expressed as the sum of its steady-state value and a small perturbation (e.g., $x = x_0 + \Delta x$). By substituting these expressions into the Taylor expansion, a set of linear expressions is obtained (e.g., $\Delta f(x_i) = \sum \frac{\partial f}{\partial x_i}\big|_{x_0} \Delta x_i$) [35]. These linear equations help derive the impedance models and indicate the system's response to small disturbances.

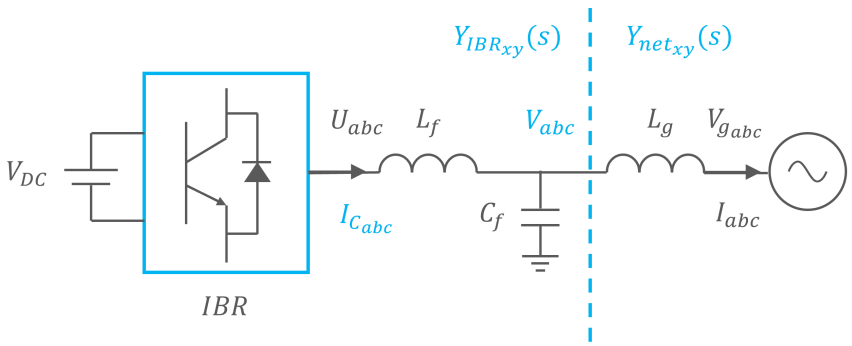

Figure 3.1: Typical single IBR connected to the grid.

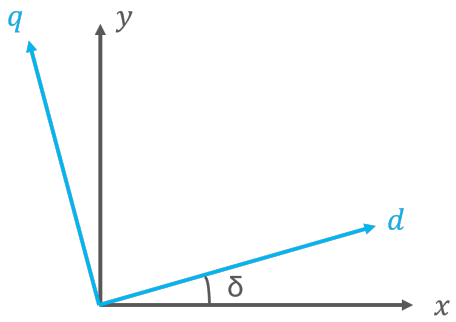

Figure 3.2: Relationship between the local and the global reference frames.

For the grid side, the linearised equations in the s-domain are represented in equation 3.1.

$$\begin{bmatrix}\Delta I_x \\ \Delta I_y\end{bmatrix} = \mathbf{Y}_{\text{net\_xy}}(s) \begin{bmatrix}\Delta V_x \\ \Delta V_y\end{bmatrix} \tag{3.1}$$

The x and y axes represent components in the global reference frame. ΔV_x and ΔV_y are the changes in terminal voltage, while ΔI_x and ΔI_y are the corresponding changes in injected current. $Y_{\text{net\_xy}}$ is the admittance matrix of the grid.

For the IBR side, the linearised equations of voltage and current are given in equation 3.2.

$$\begin{bmatrix}\Delta I_d \\ \Delta I_q\end{bmatrix} = -\mathbf{Y}_{\text{IBR\_dq}}(s) \begin{bmatrix}\Delta V_d \\ \Delta V_q\end{bmatrix} \tag{3.2}$$

The d and q axes are the components in the local reference frame. The negative sign indicates that the current from the PCC to the IBR flows in the opposite direction of the injected current to the grid. $Y_{\text{IBR\_xy}}$ is the admittance matrix of the IBR, describing the current response to a small voltage perturbation.

As seen in equation 3.1 and equation 3.2, the two systems operate in different frames: global and local. The IBR is described in the dq local frame due to the PLL-based control loops, while the global frame operates at a fixed nominal grid frequency. To obtain the full closed-loop transfer function of the system, we must transform the local coordinates into the global frame. This relationship is shown in figure 3.2. Under steady-state conditions, the d-axis is assumed to be aligned with the terminal voltage V_{abc}.

To perform this transformation, we use the rotation matrix shown in equation 3.18.

$$\mathbf{Y}_{\text{IBR\_xy}}(s) = T^{-1}\mathbf{Y}_{\text{IBR\_dq}}(s)T, \quad T = \begin{bmatrix}\cos\delta & \sin\delta \\ -\sin\delta & \cos\delta\end{bmatrix} \tag{3.3}$$

This yields the linearised equations for the IBR in the global x-y frame, as shown in equation 3.4.

$$\begin{bmatrix}\Delta I_x \\ \Delta I_y\end{bmatrix} = -\mathbf{Y}_{\text{IBR\_xy}}(s) \begin{bmatrix}\Delta V_x \\ \Delta V_y\end{bmatrix} \tag{3.4}$$

Based on equation 3.1 and equation 3.4, we derive the multiple-input multiple-output (MIMO) closed-loop control system shown in figure 3.3. The transfer function of the closed-loop system is given in equation 3.5. This formulation allows us to assess small-signal stability: if the zeros of the denominator $I + Y_{IBR}Y_{net}^{-1}$ lie in the left-half of the complex plane, the system is stable. Note that these are matrix transfer functions, as they capture both components of the reference frame.

$$CL(s) = \frac{Y_{IBR\_xy}(s)}{I + Y_{IBR\_xy}(s)Y_{net\_xy}^{-1}} \tag{3.5}$$

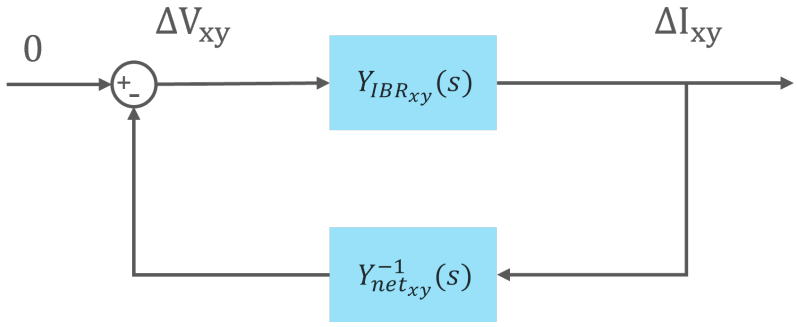

Figure 3.3: Diagram of the MIMO closed-loop control system of grid-connected IBR.

To conduct the small-signal analysis, the IBR and grid impedance matrices must be derived, as presented in the following sections.

3.2. Admittance Matrix of the Grid for Single Connected IBR

We apply a perturbation in the grid side equations in the s domain:

$$\begin{aligned} \Delta V_x &= sL_g\Delta I_x - \omega L_g \Delta I_y \\ \Delta V_y &= sL_g\Delta I_y + \omega L_g \Delta I_x \end{aligned} \tag{3.6}$$

By transforming equation 3.9 in matrix format can generate the Z_{net_xy} matrix. By getting the inverse of this matrix, we get the admittance matrix of the grid as expressed in equation 3.8, where $\omega = 2\pi f$ and f the nominal frequency of the grid.

$$\begin{bmatrix} \Delta V_x \\ \Delta V_y \end{bmatrix} = \begin{bmatrix} sL_g & -\omega L_g \\ \omega L_g & sL_g \end{bmatrix} \begin{bmatrix} \Delta I_x \\ \Delta I_y \end{bmatrix} \Rightarrow \begin{bmatrix} \Delta V_x \\ \Delta V_y \end{bmatrix} = Z_{net\_xy} \begin{bmatrix} \Delta I_x \\ \Delta I_y \end{bmatrix} \tag{3.7}$$

$$Y_{net\_xy} = Z^{-1}_{net\_xy} = \frac{1}{\omega L_g} \begin{bmatrix} \frac{\omega s}{s^2+\omega^2} & \frac{\omega^2}{s^2+\omega^2} \\ -\frac{\omega^2}{s^2+\omega^2} & \frac{\omega s}{s^2+\omega^2} \end{bmatrix} \tag{3.8}$$

3.3. Admittance Model of GFL Inverter

In this section the admittance model of a GFL IBR is derived. The GFL control is the one depicted in figure 3.4. The control includes the PLL, the Power Control (PC) and the Current Control (CC).

Beginning with the physical circuit, the voltage low at the inverter side is given as follows:

$$\begin{aligned} U_d &= sL_f i_d - \omega L_f i_q + V_d \\ U_q &= sL_f i_q + \omega L_f i_d + V_q \end{aligned} \tag{3.9}$$

where i_d, i_q the currents injected from the inverter, U_d, U_q the voltage at the inverter before the filter, V_d, V_q the terminal voltages and L_f is the inductance of the LC filter.

The control law of the current is:

$$\begin{aligned} U^*_d &= PI_{CC}(s)(i_{d,ref} - i_d) - \omega L_f i_q + f_{VF} V_d \\ U^*_q &= PI_{CC}(s)(i_{q,ref} - i_q) + \omega L_f i_d + f_{VF} V_q \end{aligned} \tag{3.10}$$

where $PI_{CC}(s) = K_p + K_i/s$ the transfer question for the PI controller, $f_{VF}(s) = K_{VF}/(sT_{VF} + 1)$ a low pass filter for the feed-forward voltage.

By combining equation 3.9 and equation 3.10 we obtain:

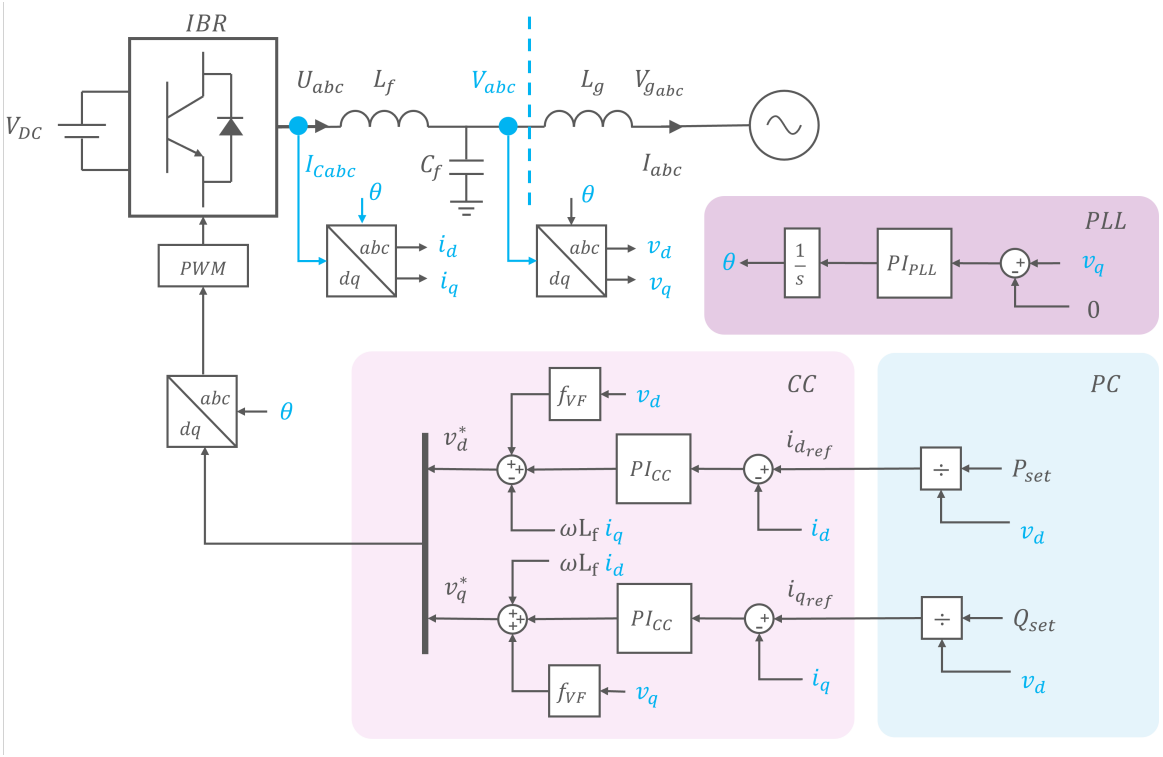

Figure 3.4: Control Diagram of GFL control.

$$\begin{aligned} i_d &= G_I(s) i_{d,ref} - Y_{VF}(s) V_d \\ i_q &= G_I(s) i_{q,ref} - Y_{VF}(s) V_q \end{aligned} \tag{3.11}$$

where:

$$G_I(s) = \frac{PI_{cc}(s)}{sL_f + PI_{cc}(s)},\ Y_{VF}(s) = \frac{1 - f_{VF}}{sL_f + PI_{cc}(s)} \tag{3.12}$$

The PLL dynamics follow:

$$\theta = \frac{PI_{PLL}(s)}{s} V_q \Rightarrow \Delta\theta = \frac{PI_{PLL}(s)}{s} \Delta V_q \tag{3.13}$$

where $PI_{PLL}(s) = K_{PLL,p} + K_{PLL,i}/s$ is the transfer function for the PI controller for the PLL.

Next, the references for the currents are given by the Power Controller. The references are calculated by equation 3.14. Since $V_q = 0$ from the PLL, the references are calculated as follows:

$$\begin{aligned} i_{d,ref} &= \frac{2}{3} \frac{P_{set}}{V_d} \\ i_{q,ref} &= \frac{2}{3} \frac{Q_{set}}{V_d} \end{aligned} \tag{3.14}$$

By linearising equation 3.14 around the steady state, we obtain:

$$\begin{aligned} \Delta i_{d,ref} &= -\frac{2}{3} \frac{P_{set}}{V_{d0}^2} \\ \Delta i_{q,ref} &= -\frac{2}{3} \frac{Q_{set}}{V_{d0}^2} \end{aligned} \tag{3.15}$$

where V_{d0} is the value of the d-axis at the steady state.

We assume that $Q_{set} = 0$. By applying a perturbation in equation 3.11 and substituting equation 3.15, we obtain the admittance model of the GFL inverter in the local d-q frame as shown in equation 3.16.

$$\begin{bmatrix} \Delta I_{Cd} \\ \Delta I_{Cq} \end{bmatrix} = - \begin{bmatrix} Y_{11} & Y_{12} \\ Y_{21} & Y_{22} \end{bmatrix} \begin{bmatrix} \Delta V_d \\ \Delta V_q \end{bmatrix} \tag{3.16}$$

where:

$$\begin{aligned} Y_{11}(s) = \frac{G_I(s) P_{\text{set}}}{V_{d0}^2} + Y_{VF}(s), \qquad Y_{12}(s) = 0 \\ Y_{21}(s) = \frac{G_I(s) Q_{\text{set}}}{V_{d0}^2}, \qquad Y_{22}(s) = Y_{VF}(s) \end{aligned} \tag{3.17}$$

As discussed in the previous section, the admittance matrix needs to be transformed to the global x-y frame. Assuming that the angle at the global frame is θ_G and in the local θ. The difference between these two is $\delta = \theta - \theta_G$. That in small signal is equal to $\Delta\delta = \Delta\theta$, since in the global frame $\Delta\theta_G = 0$. Based on that, the voltages and the currents in the global x-y coordinates are the corresponding vectors if rotated by δ:

$$\begin{bmatrix} V_x \\ V_y \end{bmatrix} = e^{J\delta} \begin{bmatrix} V_d \\ V_q \end{bmatrix} \tag{3.18}$$

where:

$$J = \begin{bmatrix} 0 & -1 \\ 1 & 0 \end{bmatrix} \Rightarrow e^{J\delta} = \begin{bmatrix} cos\delta & -sin\delta \\ sin\delta & cos\delta \end{bmatrix} \tag{3.19}$$

After linearising equation 3.18 around the steady state, we obtain:

$$\begin{bmatrix} \Delta V_x \\ \Delta V_y \end{bmatrix} = e^{J\delta_0} \begin{bmatrix} \Delta V_d \\ \Delta V_q \end{bmatrix} + J e^{J\delta_0} \begin{bmatrix} V_{d0} \\ V_{q0} \end{bmatrix} \Delta\delta = e^{J\delta_0} \left(\begin{bmatrix} \Delta V_d \\ \Delta V_q \end{bmatrix} + \begin{bmatrix} -V_{q0} \\ V_{d0} \end{bmatrix} \Delta\delta \right) \tag{3.20}$$

Similarly, we obtain for the currents:

$$\begin{bmatrix} \Delta I_{Cx} \\ \Delta I_{Cy} \end{bmatrix} = e^{J\delta_0} \left(\begin{bmatrix} \Delta I_{Cd} \\ \Delta I_{Cq} \end{bmatrix} + \begin{bmatrix} -I_{Cq0} \\ I_{Cd0} \end{bmatrix} \Delta\delta \right) \tag{3.21}$$

By adding the small signal PLL dynamics from equation 3.13 (remember $\Delta\delta = \Delta\theta$) into equation 3.20 and equation 3.21 and mathematical manipulations we obtain:

$$\begin{bmatrix} \Delta I_{Cx} \\ \Delta I_{Cy} \end{bmatrix} = -Y_{C_{GFL}\_xy}(s) \begin{bmatrix} \Delta V_x \\ \Delta V_y \end{bmatrix} \tag{3.22}$$

where

$$Y_{C_{GFL}\_xy}(s) = e^{J\delta_0} \begin{bmatrix} Y_{11}(s) & \dfrac{sY_{12}(s) + P_{PLL}(s) I_{Cq0}}{s + P_{PLL}(s) V_{d0}} \\ Y_{21}(s) & \dfrac{sY_{22}(s) - P_{PLL}(s) I_{Cd0}}{s + P_{PLL}(s) V_{d0}} \end{bmatrix} e^{-J\delta_0} \tag{3.23}$$

At steady state, we assume $\delta_0 = 0 \Rightarrow e^{J_0} = 1$ and $I_{Cq0} = 0$ [9], so the above matrix can be further simplified. However, this admittance matrix is seen from the filter side. To define it from the grid side, we need to add the admittance matrix of the capacitor C_f of the LC filter. Thus:

$$Y_{GFL\_xy}(s) = Y_{C_{GFL}\_xy}(s) + Y_c(s) \tag{3.24}$$

where:

$$Y_c(s) = \begin{bmatrix} sC_f & -\omega C_f \\ \omega C_f & sC_f \end{bmatrix} \tag{3.25}$$

3.4. Admittance model of GFM inverter

In this section, the admittance model of a GFM IBR is derived. The control scheme for the GFM is depicted in figure 3.5. As can be seen, the VSM scheme without reactive power control is implemented. The internal frequency of the controller is generated by emulating the swing equation, as seen in equation 3.31 and using the active power signal. J is the virtual inertia and D the virtual damping coefficeint. The current references are, in this case, calculated by the voltage control loop.

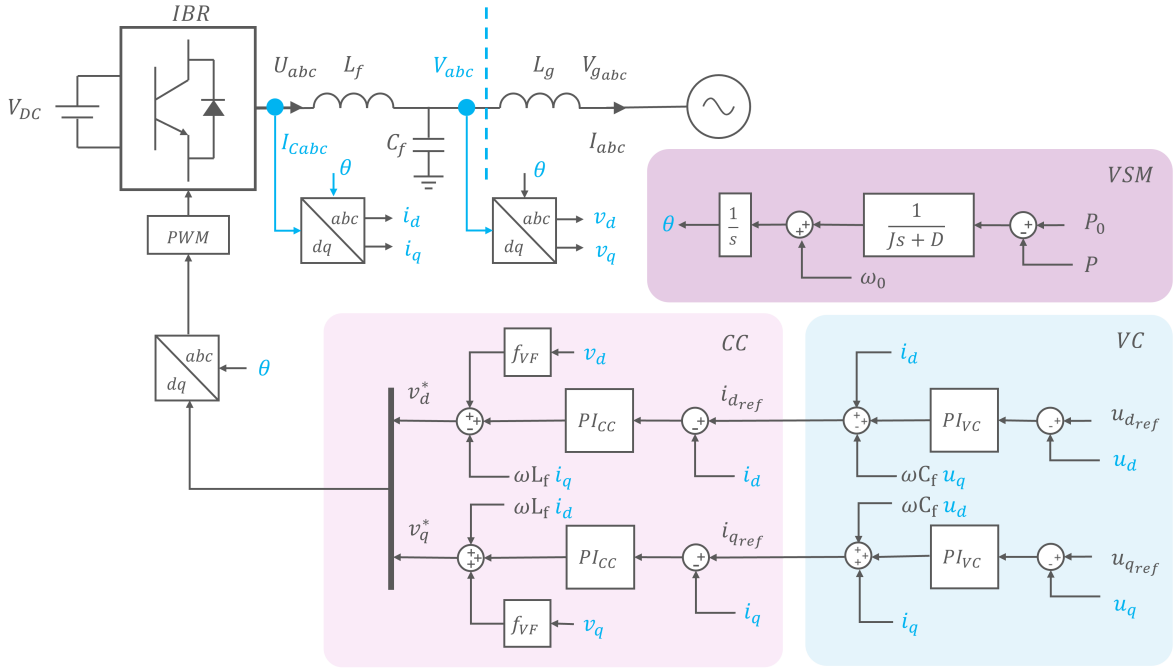

Figure 3.5: Control Diagram of GFM control utilising VSM.

$$f_{swing}(s) = \frac{1}{Js + D} \tag{3.26}$$

All the equations for the physical network and the current control are the same as in the GFL control, as seen in equation 3.9 and equation 3.10. The current law in the capacitor of the LC filter gives:

$$\begin{aligned} i_{Cd} - i_d &= sC_f V_d - \omega C_f V_q \\ i_{Cq} - i_q &= sC_f V_q + \omega C_f V_d \end{aligned} \tag{3.27}$$

For the voltage control loop, the control loop is shown in equation 3.28.

$$\begin{aligned} i_{d,ref} &= PI_{VC}(s)(u_{d,ref} - u_d) - \omega C_f i_q + f_{CF}(s) i_d \\ i_{q,ref} &= PI_{VC}(s)(u_{q,ref} - u_q) + \omega C_f i_d + f_{CF}(s) i_q \end{aligned} \tag{3.28}$$

where $PI_{VC}(s) = K_{P,VC} + K_{I,VC}/s$ is the the PI controller for the voltage and f_{CF} the low pass filter for the current feed-forward.

By combining equation 3.28 with equation 3.27 and equation 3.11 we obtain the admittance matrix for the controller in the dq frame as seen below:

$$-\begin{bmatrix}\Delta I_{Cd}\\ \Delta I_{Cq}\end{bmatrix} = \begin{bmatrix}Y_0(s) & 0\\ 0 & Y_0(s)\end{bmatrix}\begin{bmatrix}\Delta V_d\\ \Delta V_q\end{bmatrix}. \tag{3.29}$$

where:

$$Y_0(s) = \frac{Y_{VF}(s) + G_I(s)PI_{VC}(s) + G_I(s)sC_F}{1 - G_I(s)}. \tag{3.30}$$

As done in the GFL control, the local dq frame must be transformed to the global xy frame. In this case, the angular velocity is given by the swing equation. The small signal equation of the swing equation is:

$$\Delta\delta = -\frac{1}{Js^2 + Ds}\Delta P_E. \tag{3.31}$$

By using equation 3.20 and equation 3.21 and equation 3.31 we obtain the model of the controller in the xy frame:

$$\begin{bmatrix}\Delta I_{Cx}\\ \Delta I_{Cy}\end{bmatrix} = Y_{C_{GFM}\_xy}(s)\begin{bmatrix}\Delta V_x\\ \Delta V_y\end{bmatrix} \Rightarrow \begin{bmatrix}\Delta I_{Cx}\\ \Delta I_{Cy}\end{bmatrix} = \begin{bmatrix}Y_0(s) & 0\\ \frac{I_{Cd0}^2 - Y_0^2(s)V_{d0}^2}{Js^2+Ds} & Y_0(s)\end{bmatrix}\begin{bmatrix}\Delta V_x\\ \Delta V_y\end{bmatrix} \tag{3.32}$$

Once again, the admittance model from the filter side by adding the capacitor matrix:

$$Y_{GFM\_xy}(s) = Y_{C_{GFM}\_xy}(s) + Y_c(s) \tag{3.33}$$

3.5. Voltage Source behaviour of GFL and GFM inverters

The impedance/admittance models that were used in the previous analysis are very useful since they offer compact visualisation and give information about the interactions between the different control loops. Apart from that, they can be used to analyse the voltage source behaviour of the GFL and GFM inverters. As mentioned in [9], from a small-signal dynamics perspective, a GFM converter can be represented as an ideal voltage source (infinite bus) in series with an equivalent internal inductance at the node where AC voltage control is applied. In figure 3.6, the impedance model of an inverter, with either GFL or GFM control, is shown, connected to the ac grid via an impedance $Z_g(s)$. Behind the impedance, it is an ideal voltage source. This way, this impedance represents the ”distance” between the voltage at the PCC and the ideal voltage source. Note that even if in the beginning it was mentioned that GFL control can be represented as a current source in parallel to an impedance, based on Norton’s theorem, any current source can also be a voltage source. If $Z_{GFL} = 0$ or $Z_{GFM} = 0$ then the inverter can be considered as an ideal voltage source. That means that $\begin{bmatrix}\Delta V_x & \Delta V_y\end{bmatrix}^T = 0$ meaning that the voltage stays constant to any change in the current, like an infinite grid.

This approach is presented in the work of Xin et al. [9], and it is a valuable tool since, as discussed in the definition of gSCR, in the grounded Laplacian matrix the ideal voltage sources are grounded. This means that any inverter can be represented as a perfect voltage source in series with an impedance. The lower the impedance, the closer the behaviour is to that of a perfect voltage source. However, it is nontrivial to measure the impedance of a GFL or GFM inverter since it is a 2×2 transfer function matrix. In the paper, by performing singular value decomposition, the authors manage to characterise the magnitudes of the GFL and GFM impedances. In practice, by calculating the largest singular value of the impedance matrix $\overline{\sigma}(Z(j\omega))$ (or equivalently the smallest of the admittance matrix), the distance from ideal voltage-source behaviour can be quantified. A large value of $\overline{\sigma}(Z(j\omega))$ indicates that $Z(s)$ is large in a certain direction where the inverter’s behaviour deviates significantly from that of an ideal

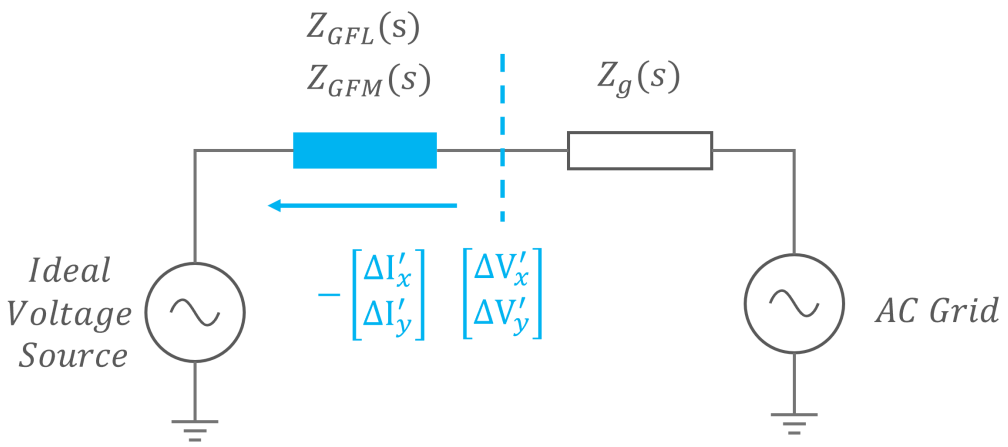

Figure 3.6: Impedance model and ideal voltage source.

voltage source. Conversely, a small $\overline{\sigma}(Z(j\omega))$ shows that the inverter is close to ideal voltage-source behaviour.

In figure 3.7 from [9], the maximum singular values of various inverter control strategies are shown in the frequency domain. As can be seen, the GFL exhibits the largest singular values, indicating the worst voltage-source behaviour. The $\overline{\sigma}(Z_{GFM}(j\omega))$ corresponds to GFM control with VSM without Q-droop, as developed previously in section 3.4. $\overline{\sigma}(Z_{GFM-QD}(j\omega))$ represents VSM with Q-droop, $\overline{\sigma}(Z_{PI}(j\omega))$ corresponds to GFM with power-synchronization control, and $\overline{\sigma}(Z_{droop}(j\omega))$ to GFM with droop control. In addition, $\overline{\sigma}(Z_{GFM-VI}(j\omega))$ and $\overline{\sigma}(Z_{GFM-damp}(j\omega))$ correspond to GFM with virtual impedance and damping control, respectively. It is evident that all GFM inverters exhibit behaviour closer to that of an ideal voltage source.

3.6. Power Networks Modelling

We assume an electrical network with multiple lines and nodes, like the one in figure 3.8, where m IBR are interconnected between them. The network consists of three types of nodes: m IBRs nodes that can be either GFL or GFM (nodes denoted $1 \sim m$), n internal nodes (denoted $m+1 \sim m+n$) and k infinite grid buses (denoted $m+n+1 \sim m+n+k$). At least one infinite bus is needed to be present in the network in order to give the frequency reference for the PLLs. The infinite bus can represent a connection to the rest of the grid or some big capacity generation [9].

Before we proceed we need to mention the following assumptions [36]:

1. We assume all transmission lines are mainly inductive, which means that the ratio $\tau = R/L$ is small and same value for every line in the network.
2. We assume that all the IBRs are adopting the same control strategy and with the same parameters, meaning that they have the same admittance model.

The network topology can be described as a weighted undirected graph, where edges represent transmission lines connecting various vertices, and the vertices represent the buses. The weights correspond to the susceptances of the lines connecting the buses.

3.6.1. Graph theory basics

In general, in graph theory, for every graph $G = (V, E)$ with V vertices and E edges, we define the following matrices [37].

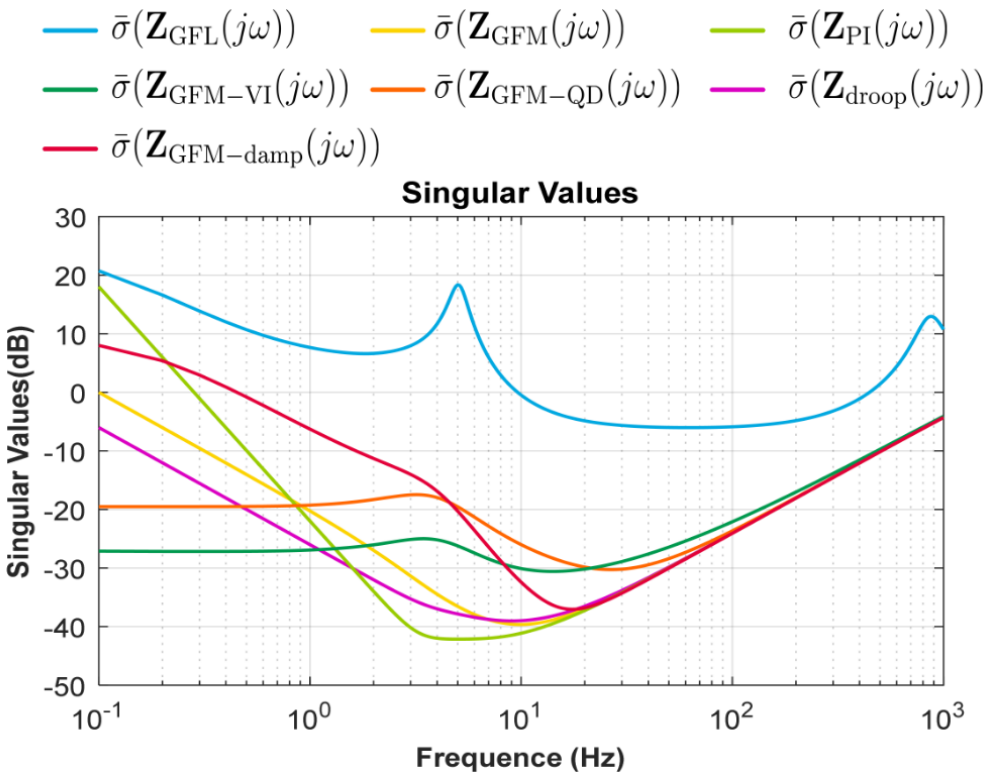

Figure 3.7: The largest singular values of the impedance matrices of various inverter controls [9].

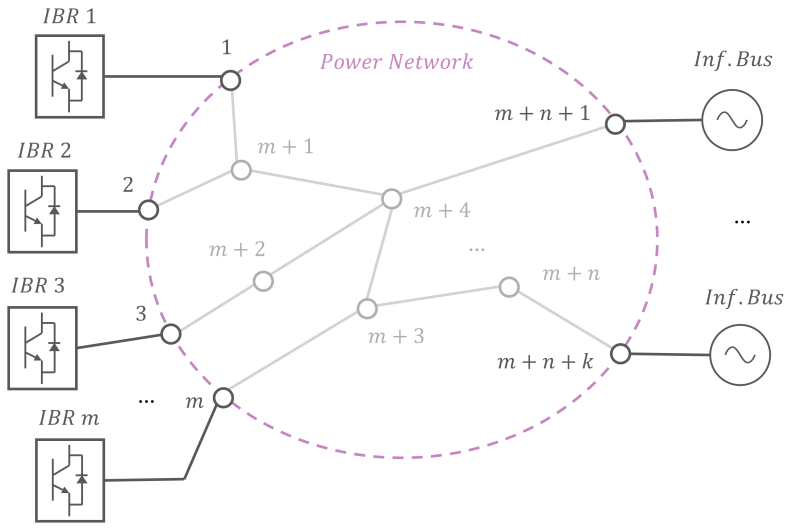

Figure 3.8: An electrical network with multiple IBRs connected.

The *adjacency matrix* A of a graph with N nodes is defined as

$$A_{ij} = \begin{cases} 1, & \text{if node } i \text{ is connected to node } j, \\ 0, & \text{otherwise.} \end{cases} \tag{3.34}$$

In the case of weighted graphs, such as power networks where lines have susceptances B_{ij}, we set

$$A_{ij} = B_{ij} \tag{3.35}$$

to represent the weight of the edge between nodes i and j.

The *degree matrix* D is a diagonal matrix whose i-th diagonal element represents the sum of the weights of all edges connected to node i, i.e.,

$$D_{ii} = \sum_{j=1}^{N} A_{ij}. \tag{3.36}$$

For unweighted graphs, D_{ii} simply counts the number of edges incident to node i. For weighted power networks, D_{ii} represents the total susceptance connected to node i.

The *Laplacian matrix* L is defined as

$$L = D - A. \tag{3.37}$$

The Laplacian matrix is symmetric and positive semidefinite for undirected graphs and it captures the overall connectivity structure and plays a key role in analyzing power flows and stability.

3.6.2. The Grounded Laplacian Matrix

To model small signal interactions in the network, we use the concept of the *grounded Laplacian matrix* Q. This matrix characterizes the connectivity and coupling strength between the nodes (especially between the generation nodes) in the network. The grounded Laplacian is generated by removing the rows and columns of L corresponding to the grounded vertices [38]. In the case of power networks and for small signal stability, the buses connected to the infinite buses can be grounded [30], since small perturbations will not cause any changes to such strong buses.

For $i \neq j$ among the free nodes, the (i, j) entry of Q is

$$Q_{ij} = -B_{ij}, \tag{3.38}$$

where $B_{ij} = 1/\omega L_{ij}$ the negative of the susceptance between nodes i and j.

The diagonal elements are defined so that each row sums to zero (reflecting Kirchhoff's current law),

$$Q_{ii} = \sum_{\substack{j=1 \\ j \neq i}}^{m+n+k} B_{ij} + B_{i,\text{inf}}, \tag{3.39}$$

where $B_{i,\text{inf}}$ is the susceptance connecting node i to any infinite bus (ground).

In other words, Q_{ii} equals the sum of all line susceptances incident at node i, including connections from i to an infinite bus node. By construction, Q is a symmetric positive semi-definite matrix [30].

3.6.3. Kron Reduction

Apart from grounding the infinite buses, the interior nodes will be eliminated by assuming that the currents injected into these nodes remain constant during small signal perturbations [30]. This is done by conducting Kron reduction [39] as seen in figure 3.9. As can be seen, the IBRs interact with each other through the equivalent network, and the self-loops reflect the interactions between them and the infinite buses.

The grounded Laplacian matrix of the Kron-reduced network can be calculated as follows [36]:

$$Q_{\text{red}} = Q_1 - Q_2 Q_4^{-1} Q_3, \tag{3.40}$$

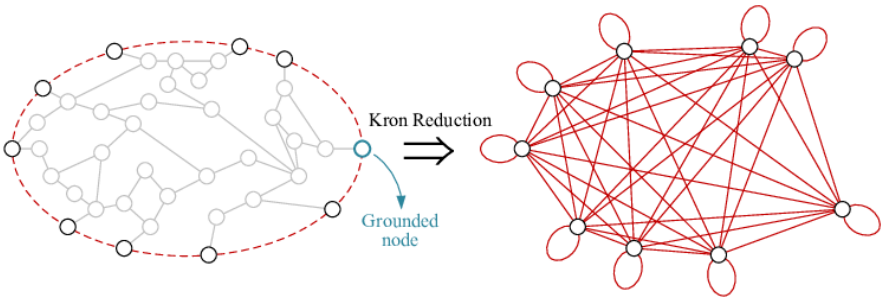

Figure 3.9: Kron Reduction [36].

where

$$Q_1 \in \mathbb{R}^{m\times m}, \quad Q_2 \in \mathbb{R}^{m\times n}, \quad Q_3 \in \mathbb{R}^{n\times m}, \quad Q_4 \in \mathbb{R}^{n\times n}$$

are the submatrices of Q defined as

$$Q = \begin{bmatrix} Q_1 & Q_2 \\ Q_3 & Q_4 \end{bmatrix}. \tag{3.41}$$

Submatrix $Q_1 \in \mathbb{R}^{m\times m}$ corresponds to couplings among the IBR nodes, $Q_4 \in \mathbb{R}^{n\times n}$ is the submatrix for couplings among interior nodes and $Q_2 = Q_3^T$ captures connections between generator and interior nodes.

3.7. Generalized Short Circuit Ratio (gSCR)

The SCR index is a widely used metric to quantify the strength of a grid at the point of common coupling for a single IBR-connected system. For systems with multiple inverters connected to a shared grid, the interactions among converters and the network can no longer be captured accurately using individual SCR values. To address this limitation, Dong *et al.* [11] introduced the concept of the generalised Short Circuit Ratio (gSCR), which generalises the idea of SCR to multiple IBR-connected systems.

The gSCR of the system depicted in figure 3.8 is defined as the smallest eigenvalue of the $S_B^{-1}Q_{red}$ as shown below:

$$\mathrm{gSCR} = \lambda_{\min}(S_B^{-1}Q_{red}) = \lambda_{\min}(Y_{eq}), \tag{3.42}$$

where $S_B \in \mathbb{R}^{n\times n}$ is a diagonal matrix whose $i-th$ element is the ratio of the power rating of the $i-th$ IBR S_i over the global power base S_{global} and Y_{eq} is also refered to the literature as the extended admittance matrix.

The calculation of the gSCR requires knowledge of both the network parameters, including the topology and line impedances, and the rated capacities of the various generations. As such, gSCR serves as a system-level metric that characterizes the strength of the grid in a multi-converter system. From a mathematical perspective, the gSCR captures the weighted connectivity and overall coupling strength of the power network as seen by all IBRs.

The underlying intuition of gSCR is that the power network must be sufficiently strong (low impedance lines) or the IBRs must remain close enough to ideal voltage sources (infinite buses). This enables GFL control by effectively giving the frequency references for the PLLs. From a network perspective, the gSCR can be increased, and system stability thereby enhanced, by adding more voltage sources to the network, particularly at nodes that are electrically far away from infinite buses.

The gSCR is used extensively in small-signal stability analysis of large-scale power systems. By deploying the gSCR, the stability of the network can be assessed by focusing only on the network parameters, and there is no need to compute the eigenvalues of a high-dimensional dynamic system.

Apart from that, properties of the extended admittance matrix can be used in such a way that it can decouple the multiple IBR systems into several single IBR subsystems. This way the stability of the

multiple system can be assessed based on the stability of the single IBR system. This can be done since Y_{eq} is diagonalizable and all its eigenvalues are positive, as proven in [11]. Based on that, there is a matrix W that can decompose the matrix Y_{eq} into a diagonal matrix in which the diagonal elements consist of the eigenvalues $(\lambda_i, i = 1, \ldots, n)$ in the order of $0 < \lambda_1 \leq \lambda_2 \leq \cdots \leq \lambda_n$. That is,

$$W^{-1} Y_{eq} W = \Lambda = \operatorname{diag}(\lambda_i). \tag{3.43}$$

The impact of interactions among the IBRs on the stability of a multiple IBR system can be assessed using the participation factors of the gSCR. The gSCR is defined as the smallest eigenvalue λ_1, which quantifies both the grid strength and the overall stability of the system.

The influence of each IBR on system stability can be evaluated through the extent to which it contributes to λ_1. Specifically, the participation factor p_{1j} measures how strongly the j-th IBR affects λ_1. When an IBR has a larger participation factor, it has a more significant impact on the overall system stability, indicating that its bus is weaker.

The participation factor p_{1j} is defined as

$$p_{1j} = v_{1j} u_{j1}, \tag{3.44}$$

where v_{1j} is the element in the first row and j-th column of matrix $v = W^{-1}$, which represents the left eigenvector matrix of Y_{eq}, and u_{j1} is the element in the j-th row and first column of matrix $u = W$, which represents the right eigenvector matrix of Y_{eq}.

3.8. Closed loop of the multiple grid-connected IBRs

We assume a multiple IBR power network as the one introduced in section 3.6 in figure 3.8.

For a transmission line that connects node i and node j, the dynamic equation can be expressed in the global coordinate as,

$$\begin{bmatrix} \Delta I_{x,ij} \\ \Delta I_{y,ij} \end{bmatrix} = B_{ij} F(s) \begin{bmatrix} \Delta V_{x,i} - \Delta V_{x,j} \\ \Delta V_{y,i} - \Delta V_{y,j} \end{bmatrix}, \tag{3.45}$$

where

$$F(s) = \frac{1}{(s+\tau)^2/\omega + \omega} \begin{bmatrix} s+\tau & \omega \\ -\omega_0 & s+\tau \end{bmatrix},$$

$\begin{bmatrix} \Delta I_{x,ij} & \Delta I_{y,ij} \end{bmatrix}^\top$ is the current vector from node i to node j, $\begin{bmatrix} \Delta V_{x,i} & \Delta V_{y,i} \end{bmatrix}^\top$ is the voltage at node i, $B_{ij} = 1/(L_{ij}\omega)$ is the susceptance between i and j, and τ is the identical R_{ij}/L_{ij} ratio of all the lines.

By deploying the grounded Laplacian matrix Q_{red}, where all the infinite buses are grounded and after eliminating the internal buses with Kron reduction, the network dynamics can be expressed as:

$$\begin{bmatrix} \Delta I_{x,i} \\ \Delta I_{y,i} \end{bmatrix} = Q_{red} \otimes F(s) \begin{bmatrix} \Delta V_{x,i} \\ \Delta V_{y,i} \end{bmatrix} \tag{3.46}$$

where $\begin{bmatrix} \Delta I_{x,i} & \Delta I_{y,i} \end{bmatrix}^\top$ is the current injection at node i provided by the i-th IBR.

We can stack all the current and voltage vectors for all the IBR buses to get:

$$\Delta I_{xy} = Q_{red} \otimes F(s) \times \Delta V_{xy} \tag{3.47}$$

In addition, by assuming that the IBRs are employing the same control strategy, meaning that they have the same impedance model Y_{IBR}, the stacked impedance models of all the IBRs are given as:

$$\Delta I_{xy} = -S_B \otimes Y_{IBR}(s) \times \Delta V_{xy} \tag{3.48}$$

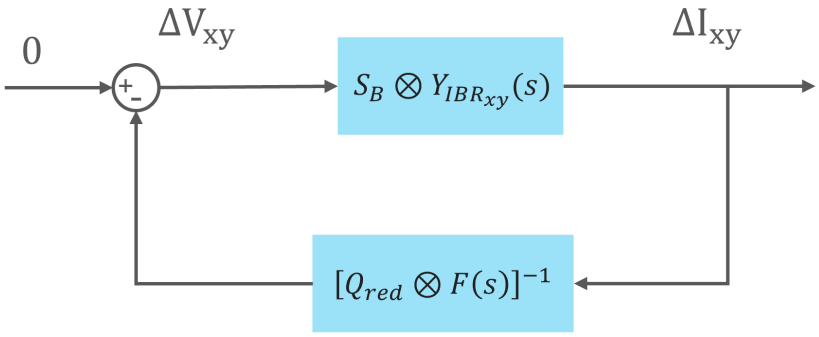

Figure 3.10: Diagram of the MIMO closed-loop control system of multiple IBR system.

where S_B is the m-dimensional diagonal matrix with the corresponding ratios of the rated capacity of each IBR over the global S_{base}. Note that $Y_{IBR}(s)$ can be the impedance models of GFLs or GFMs as derived earlier, but they must be developed at rated capacity equal to the global power base.

By combining the IBR-side dynamics (equation 3.47) with the network-side (equation 3.48), we obtain the closed-loop characteristics of the whole multiple IBR network shown in figure 3.10. The closed-loop transfer function of the whole system is given in equation 3.49.

$$CL(s) = \frac{S_B \otimes Y_{IBR}(s) \times [Q_{red} \otimes F(s)]^{-1}}{I_{2m} + S_B \otimes Y_{IBR}(s) \times [Q_{red} \otimes F(s)]^{-1}} \tag{3.49}$$

3.9. Stability analysis of multiple grid-connected IBRs

To assess the stability of a multiple IBR system, it is not necessary to calculate the poles of equation 3.49. Instead, by computing the gSCR of the network and analyzing the stability of a single IBR, the overall stability of the multiple IBR system can be evaluated.

As shown in section 3.6, the matrix Y_{eq} is diagonalizable, so as shown in equation equation 3.43 it is similar to the matrix $\Lambda = diag\{\lambda_1, \lambda_2, ..., \lambda_m\}$.

We aslo consider the following coordinate transformation

$$\begin{aligned} \Delta I_{\mathrm{T}} &= \left(T^{-1} \otimes I_2\right) \times \Delta I_{xy} \\ \Delta V_{\mathrm{T}} &= \left(T^{-1} \otimes I_2\right) \times \Delta V_{xy}, \end{aligned} \tag{3.50}$$

that makes equation 3.47 and equation 3.48 become

$$\Delta I_T = \Lambda \otimes F(s) \times \Delta V_T \tag{3.51}$$

$$\Delta I_T = -S_B \otimes Y_{IBR}(s) \times \Delta V_T \tag{3.52}$$

That means that both matrices represent the same system dynamics and share identical closed-loop poles. The previous proves that a system with m IBRs can be decoupled into m independent subsystems of single IBRs (figure 3.11). The open-loop of each subsystem i is equal to:

$$OL(s)_i = Y_{IBR}(s) \times [\lambda_i F(s)]^{-1} \tag{3.53}$$

where $0 < \lambda_1 < ... < \lambda_i < ... < \lambda_m$ are the eigenvalues of the Y_{eq}. So the multiple IBRs system is stable only if all the independent subsystems are stable [36]. However, by definition, the gSCR is the

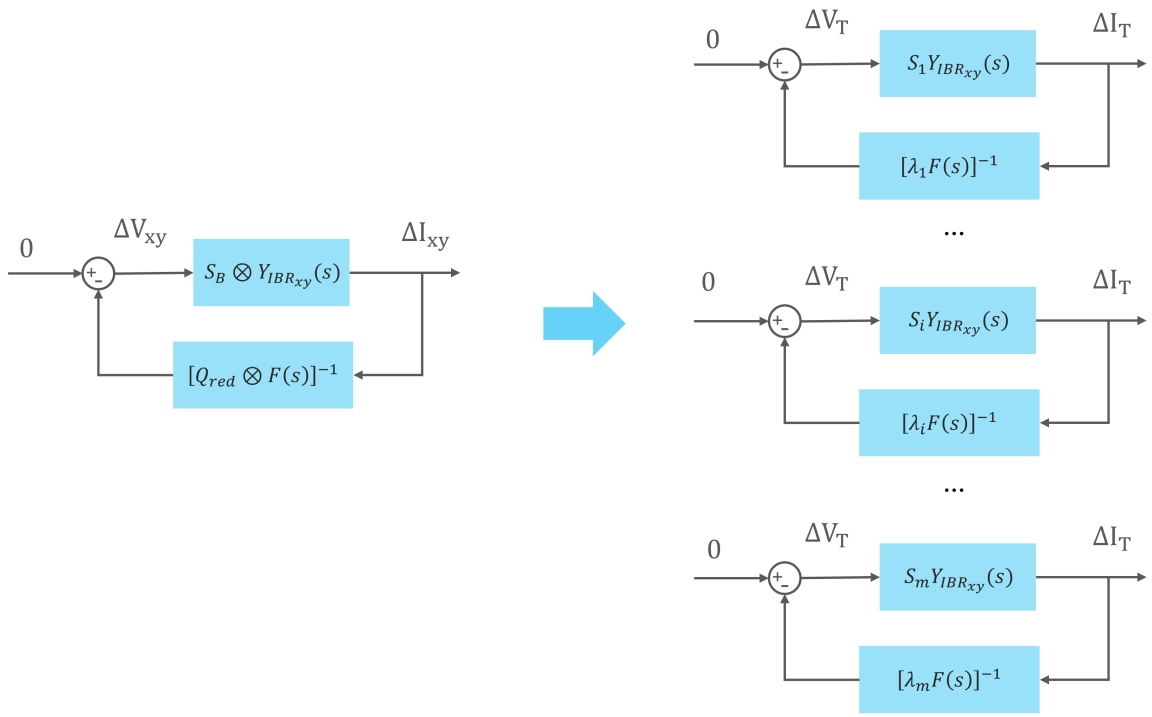

Figure 3.11: Decoupling of the multiple IBR system into individual single IBR subsystems.

smallest eigenvalue of Y_{eq}, which makes sense since if the weakest subsystem is stable, it will also be stable for the stronger ones.

Based on Dong et al. [11], the concept of the critical SCR (CSCR) can be extended to the generalized SCR (gSCR). The critical generalized SCR (CgSCR) defines the stability boundary for a multi-IBR system, meaning the system remains stable only if $gSCR > CgSCR$. When all IBRs share identical control parameters, it follows that CgSCR is equal to the CSCR of a single IBR. Therefore, once the CSCR for a single IBR has been determined (through eigenvalue analysis or simulations), it can be directly applied to assess the stability of multi-IBR systems.

4

Results by Case

This chapter presents the results case by case and links the analytical framework to time-domain evidence. Section 4.1 describes the simulation set-up in MATLAB/Simulink, and section 4.2 summarises the controller tuning. Sections 4.3-4.5 cover three cases with an infinite bus: a single GFL, a single GFM, and a GFL in parallel with a GFM. For the first two, each case pairs a concise small-signal stability assessment with representative simulations. Section 4.6 extends the analysis to multiple grid-connected IBRs. Section 4.7 presents observations across cases into discussion points and design recommendations.

4.1. Simulation Set-Up

The goal of the analysis is to assess the stability of the system under different grid strengths. To achieve this, the system is simulated in discrete time to accurately capture the controller dynamics and system transients. However, to reduce the computational burden, the Averaged Value Model of the inverter is used. This approach significantly increases simulation speed by neglecting the switching behaviour while preserving all control dynamics.

In Simulink, the three-phase inverter is modelled using three ”Half-Bridge Converters” operating in Averaged mode, as shown in figure 4.1, where the input signal is the reference voltage generated by the control system. On the DC side, the inverter is connected to a constant DC voltage source of V_{DC}.

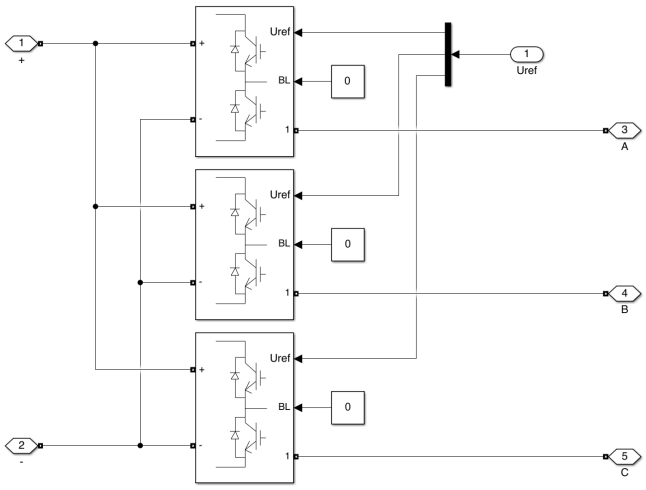

Figure 4.1: Averaged Value Model of the three-phase inverter in Simulink.

The inverter is connected to an LC filter, followed by the grid impedance, which is modelled using a ”Three-Phase Series RL Branch.” The infinite grid is represented as an ideal three-phase voltage

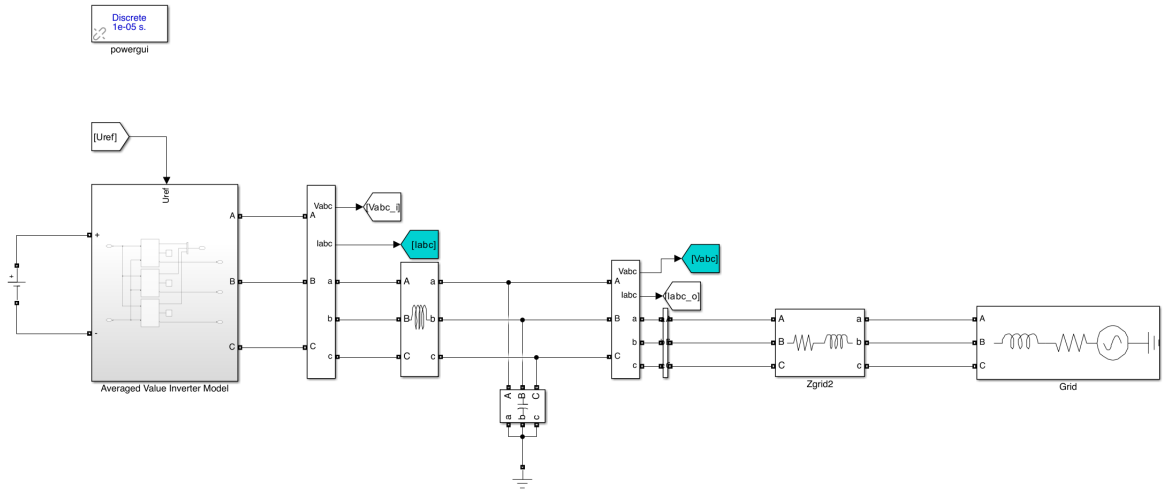

Figure 4.2: Simulink model of the inverter connected to the infinite grid.

source. Two ”Three-Phase V-I Measurement” blocks are used to measure the inverter current and the terminal phase-to-ground voltage after the LC filter. These measurements are then transformed to the d-q reference frame and used as inputs to the control system. MATLAB is using the amplitude invariant Park transform, which means that the voltage should be measured in phase-to-ground before being transformed to d-q. The whole system is shown in figure 4.2.

4.2. Tuning of the inverter's controllers

In this section, we aim to show how the PI controller gains of the GFL and GFM control were chosen. The basic idea behind controller tuning is that the control loops are well separated from each other. The outer loops are the slowest, and the inner loops are faster. That means that for the GFL, the PLL is slower than the inner control loop. For the GFM, the power synchronisation is slower, followed by the voltage control, which is faster and finally the current loop, which is the fastest. An effective way to separate them is by defining bandwidths that have one decimal difference.

First, we begin with the GFL and the tuning of the PLL. As shown in Huang et al. [32] by combining equation 3.13 with equation 3.20, we obtain the transfer function of the PLL in the global coordinates as shown in equation 4.1.

$$G_{PLL}(s) = \frac{\Delta\theta}{\Delta V_q} = \frac{1}{V_{d0}} \frac{sK_{PLL,P} + K_{PLL,I}}{s^2 + sK_{PLL,P} + K_{PLL,I}} \tag{4.1}$$

This equation reflects the second-order system of the form $s^2+2\zeta\omega_n s+\omega_n^2$, where ζ is the damping ratio of the system and ω_n is the natural frequency. Based on that, it can be calculated that $K_{PLL,P} = 2\zeta\omega_n$ and $K_{PLL,I} = \omega_n^2$. By selecting $\zeta = 1/\sqrt{2}$ for optimal performance [40], we obtain $K_{PLL,P} = \sqrt{2K_{PLL,I}}$. By choosing a controller bandwidth ω_{PLL}, which is the frequency where the magnitude of the controller transfer function is equal to -3dB, we can obtain the relation between the controller gains and the bandwidth, as shown in equation 4.2.

$$K_{PLL,I} = \frac{\omega_{PLL}^2}{2+\sqrt{5}} \tag{4.2}$$

The same procedure can be followed for the current controllers for both the GFL and GFM. The control loop can be seen in equation 4.3. For the damping ratio, we choose the $\zeta = 1$ as done in the work of Yitong Li [41] [3].

$$\frac{I_C}{I_{C,ref}} = \frac{sK_{CC,P} + K_{CC,I}}{s^2 L_f + sK_{CC,P} + K_{CC,I}} = \frac{K_{CC,P}}{Lf} \frac{s + \frac{K_{CC,I}}{K_{CC,P}}}{s^2 + s\frac{K_{CC,P}}{Lf} + \frac{K_{CC,I}}{Lf}} \tag{4.3}$$

We want the proportional term to dominate at the bandwidth. Based on that, we obtain: $K_{CC,P} = \omega_{cc} Lf$ and $K_{CC,I} = \omega_{cc}^2 Lf/4$.

4.3. Case 1: Single Grid-connected GFL Inverter

In this section, the case of a single GFL inverter connected to the infinite bus is tested. The goal is to determine the stability boundary using both impedance models and simulations.

4.3.1. Stability Analysis of Single Grid-connected GFL Inverter

Since both the grid and the GFL inverter admittance models have been developed, using equation 3.5, we can conduct the small signal analysis. The goal is to check the stability of the system for different grid strengths. We assume the same system in figure 3.4. The parameters used are shown in table 4.1. The tuning og the PLL and current loop was based on the previous section. The rest of the parameters were taken from [9].

Table 4.1: GFL inverter and Grid Parameters.

Symbol	Description	Value
f	Grid frequency	60 Hz
S_{base}	Base apparent power	1.5 MVA
V_{base}	Base line-to-line RMS voltage	690 V
V_{dc}	DC voltage	1,069 V
L_f^{pu}	Filter inductance	0.05 p.u.
C_f^{pu}	Filter capacitance	0.06 p.u.
$K_{CC,P}$	PI current controller proportional gain	188.50 p.u.
$K_{CC,I}$	PI current controller integral gain	177,650 p.u.
$K_{\text{PLL},P}$	PLL proportional gain	43.17 p.u.
$K_{\text{PLL},I}$	PLL integral gain	931.96 p.u.
T_{VF}	Voltage feedforward filter time constant	0.02 s
K_{VF}	Voltage feedforward filter gain	1
P_{set}^{pu}	Active power setpoint	1 p.u.
Q_{set}^{pu}	Reactive power setpoint	0 p.u.

To simplify the analysis, we assume that the x-axis of the global coordinate is aligned with the d-axis of the controller's coordinate at steady state, so $\delta_0 = 0$ and that the reactive power setpoint is $Q_{set} = 0$.

The poles of the closed loop transfer function equation 3.5 are calculated for different values of SCR, by increasing the line inductance, and the trajectory is generated as shown in figure 4.3. As can be seen from the figure, as the SCR becomes higher, indicating a stronger grid, the zeros are moving towards the left-hand side of the complex plane. Especially, for values of approximately $SCR > 2.3$, the poles of the system are on the left-hand side, suggesting that this value is the critical SCR (CSCR) value, which indicates the stability boundary. That means that for values lower than the $SCR < 2.3$ the zeros cross to the right-hand side of the complex plane, meaning that the system becomes unstable.

4.3.2. Simulation Results

First, the case of the GFL inverter connected to an infinite grid is considered. The simulated system is the one presented in figure 3.4, and all system parameters are listed in table 4.1. The implementation of the control in Simulink is shown in Appendix A. Note that since the average model of the inverter is used, which is controlled by $U_{ref} \in [-1, 1]$, the output of the control must be normalised by $V_{DC}/2$. Additionally, a one-step memory block is required to prevent algebraic loops.

From subsection 4.3.1 we proved that for $SCR < 2.3$ the system becomes unstable, indicating a weak grid. The simulation runs for 1.5s. For $t \leq 0.5s$ the system is strong with $SCR = 4$, for $0.5s < t \leq 1s$

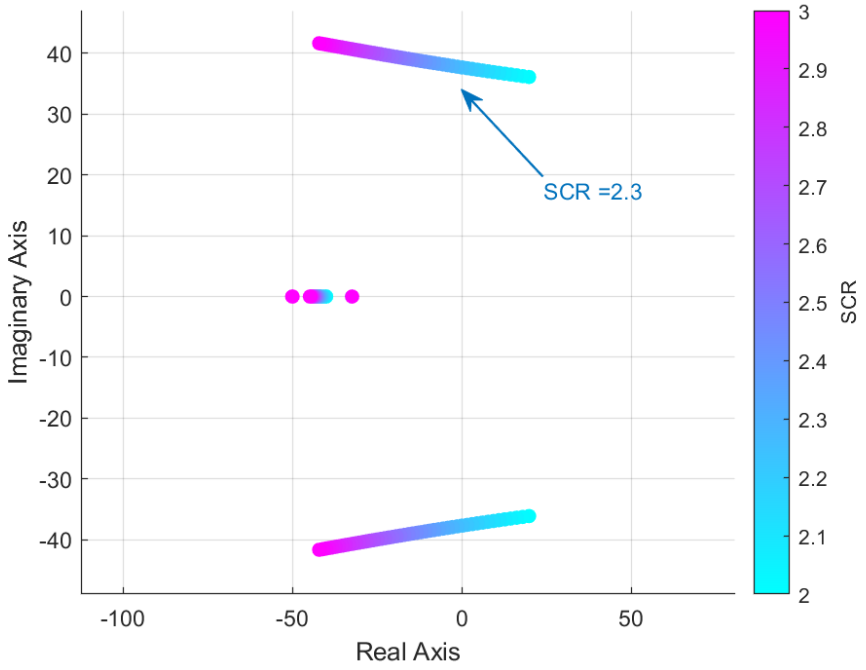

Figure 4.3: Poles trajectories of the closed-loop system for the GFL for different values of SCR.

the grid is still in the strong but very close to instability with $SCR = 3$ and for $1s < t \leq 1.5s$ the grid is considered weak with $SCR = 1.8$.

The voltage and currents in the abc frame in p.u. are shown in figure 4.4, and in the d-g frame in p.u. are shown in figure 4.5.

From the graphs, it is evident that under strong grid conditions, both voltages and currents remain stable around 1 p.u.. As the grid becomes weaker, a voltage dip is observed. Since the inverter is injecting constant power, the current must increase to compensate. In the d-q frame, we observe that the system exhibits some transients lasting approximately 0.1 seconds, but it eventually reaches a stable state. However, under very weak grid conditions (lower than the CSCR), the system becomes unstable. In the d-q frame, sustained oscillations appear around 1 p.u. on the d-axis and around zero on the q-axis, an indication that the PLL is no longer able to track accurately the grid voltage.

This confirms the findings from the literature review and the small-signal stability analysis presented in subsection 4.3.1. As the SCR approaches the CSCR, the system reaches a critical stability boundary. When the SCR falls below the CSCR, the system becomes unstable.

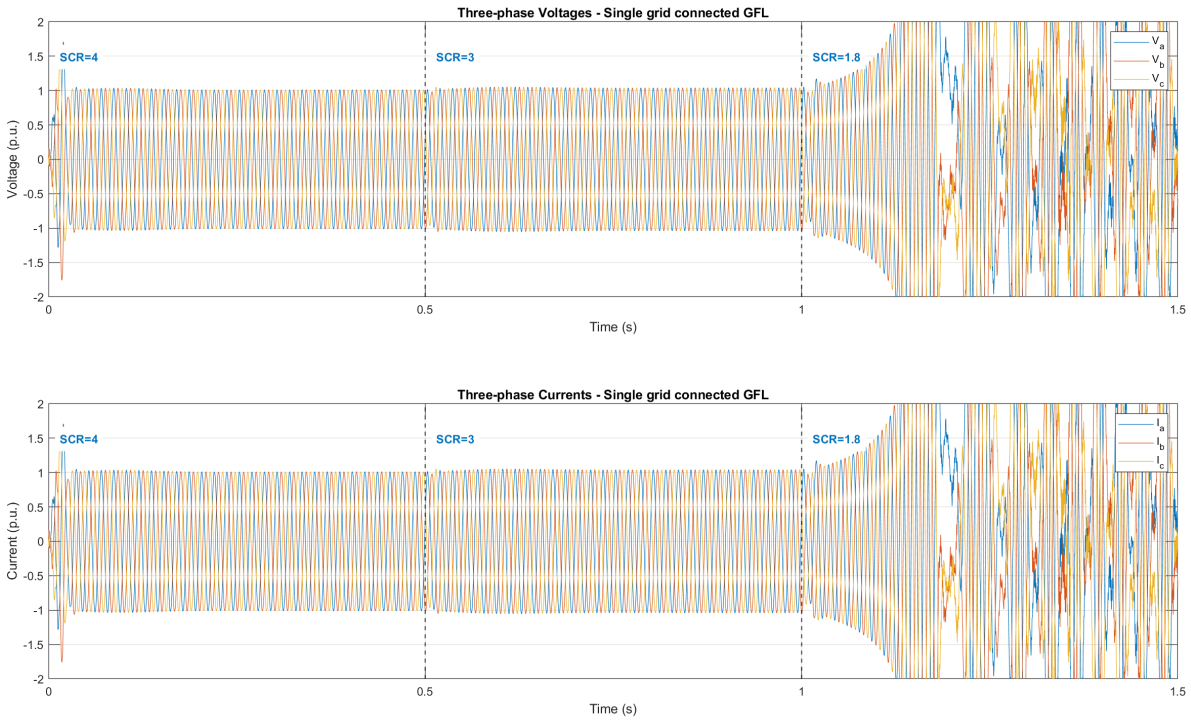

Figure 4.4: Voltages and currents of the GFL inverter under three different grid strengths.

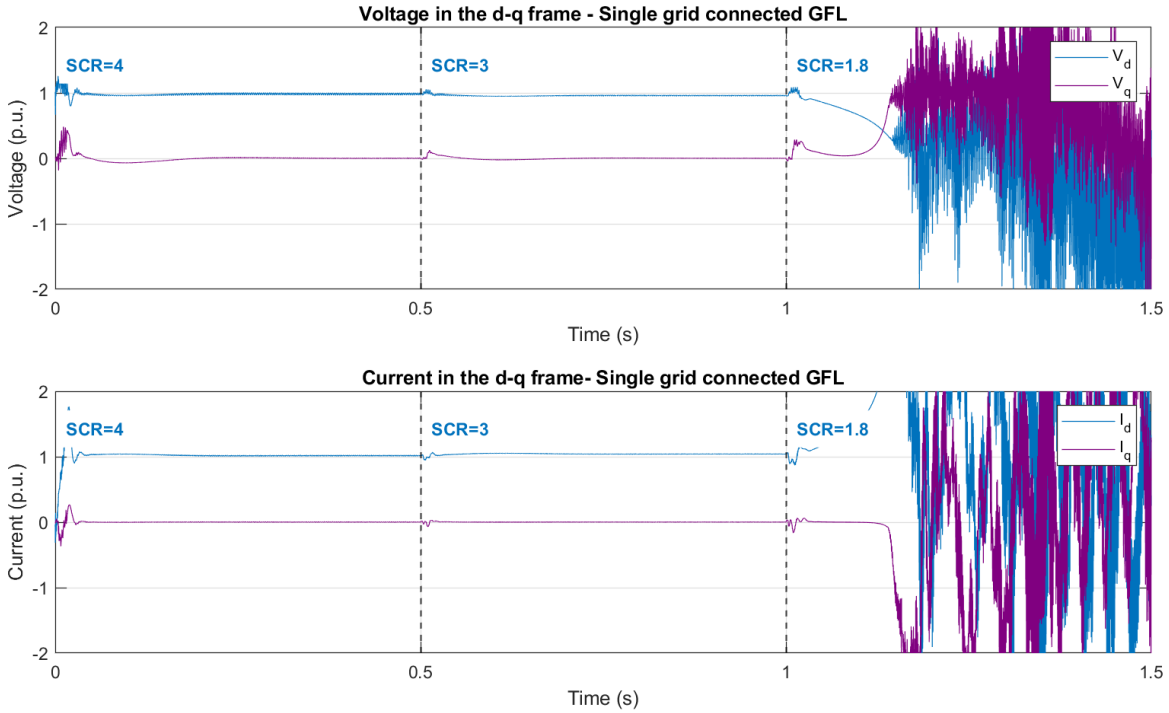

Figure 4.5: Voltages and currents in the d-q frame of the GFL inverter under three different grid strengths.

4.4. Case 2: Single grid-connected GFM inverter

In this section, the case of a GFM inverter connected to an infinite grid is examined. The simulated system configuration is shown in figure 3.5. The goal is to determine the

4.4.1. Stability analysis of single grid-connected GFM inverter

The small-signal stability of the GFM inverter tied to the infinite grid via a grid admittance can be analysed by deploying the closed-loop equation of the system and finding the poles. The parameters used for the GFM controller are listed in table 4.2. The selection of the control parameters was based on the paper [9]. The Simulink implementation of the GFM control scheme with VSM is illustrated in Appendix A.

Table 4.2: GFM inverter and Grid Parameters.

Symbol	Description	Value
f	Grid frequency	60 Hz
S_{base}	Base apparent power	1.5 MVA
V_{base}	Base line-to-line RMS voltage	690 V
V_{dc}	DC voltage	1,069 V
L_f^{pu}	Filter inductance	0.05 p.u.
C_f^{pu}	Filter capacitance	0.06 p.u.
$K_{\text{CC},P}$	PI current controller proportional gain	0.3 p.u.
$K_{\text{CC},I}$	PI current controller integral gain	10 p.u.
$K_{\text{VC},P}$	PI Voltage controller proportional gain	8 p.u.
$K_{\text{VC},I}$	PI Voltage controller integral gain	30 p.u.
J	Virtual Inertia	2
D	Virtual Damping	100
T_{VF}	Voltage feedforward filter time constant	0.02
K_{VF}	Voltage feedforward filter gain	1
P_{set}^{pu}	Active power setpoint	1 p.u.
Q_{set}^{pu}	Reactive power setpoint	0 p.u.

The zeros of the denominator in equation 3.5 are calculated for different values of SCR by increasing the line inductance, and the trajectory is generated as shown in figure 4.6. As can be seen from the figure, as the SCR becomes higher, indicating a stronger grid, the zeros move towards the right-hand side of the complex plane. Specifically, for values of approximately $SCR > 14$, the zeros of the system are on the right-hand side, suggesting that this value is the CSCR, which indicates the stability boundary. This means that for values greater than $SCR > 14$, the zeros cross to the right-hand side of the complex plane, making the system unstable. For values of $SCR < 14$, the zeros are on the left-hand side of the plane and the system is stable.

This proves the duality of GFM and GFL inverters. While GFL inverters become unstable under weak grid conditions (low SCR), GFM inverters become unstable under strong grid conditions (high SCR).

4.4.2. Simulation Results

According to the previous analysis, the GFM inverter exhibits instability at higher SCR values. Specifically, it was shown that the system becomes unstable when $SCR > 14$. In this simulation, the system is run for 1.5 s. For $t \leq 0.5\,\text{s}$, the grid is weak with $SCR = 2$. For $0.5 < t \leq 1\,\text{s}$, the SCR is increased to 5, still below the critical threshold. Finally, for $1 < t \leq 1.5\,\text{s}$, the grid strength is further increased to $SCR = 15$, exceeding the stability limit.

The voltages and currents in the abc frame in p.u. are presented in figure 4.7, and the corresponding d-q frame results are shown in figure 4.8.

From the plots, it is observed that under weak and moderate grid conditions (SCR = 2 and SCR = 5), the system operates stably with voltage and current values maintained close to 1 p.u.. The d-q frame results show that transients are damped quickly and the inverter is able to maintain stable synchronization. However, when the SCR is increased to 15, the system exhibits oscillatory behavior, and both voltage and current magnitudes become unstable. In the d-q frame, growing oscillations appear, indicating a loss of synchronization and the inability of the GFM inverter to maintain proper voltage regulation.

These simulation results are consistent with the theoretical predictions from subsection 4.4.1. As the SCR exceeds the critical value (CSCR) for the GFM inverter, the system crosses its stability boundary

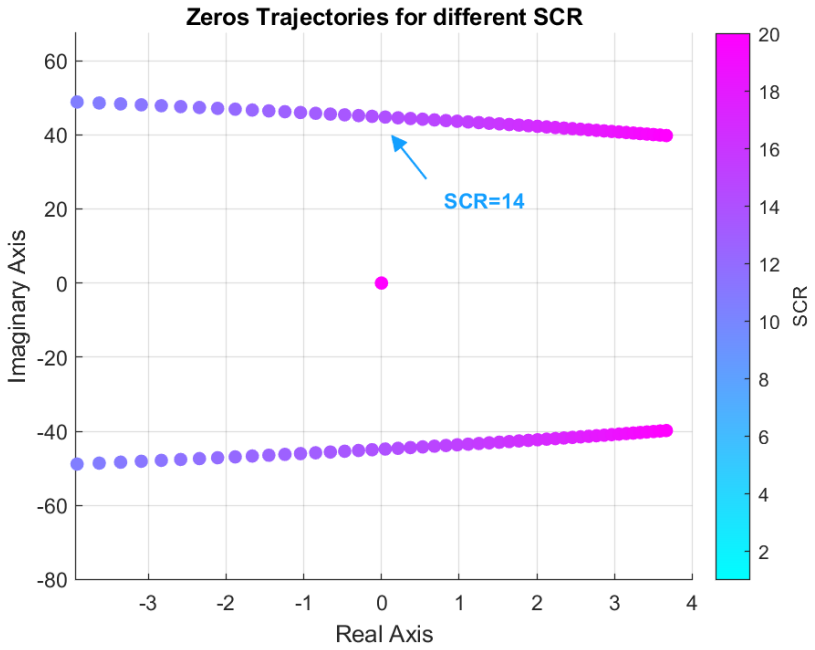

Figure 4.6: Poles trajectories of the closed-loop system for the GFM for different values of SCR.

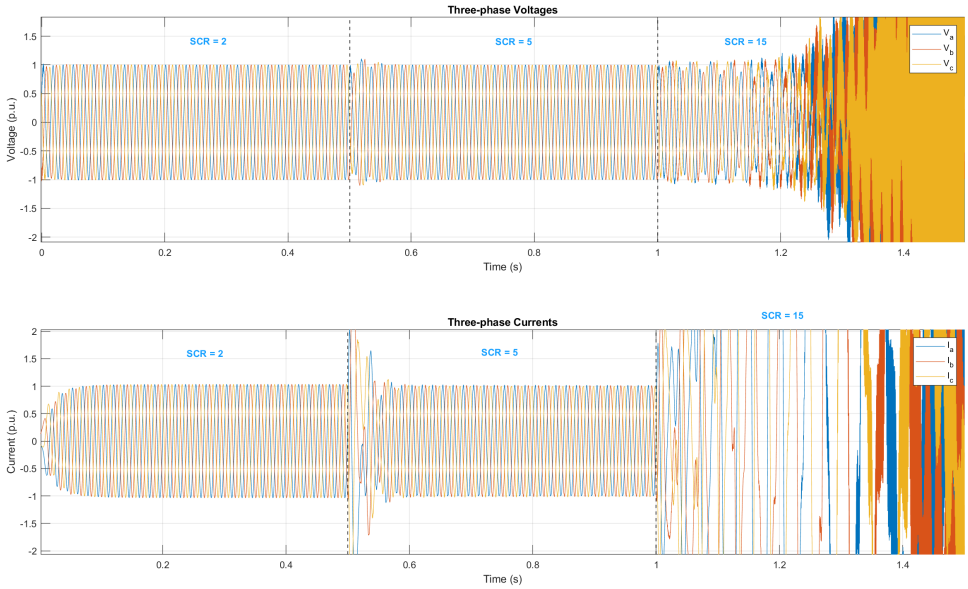

Figure 4.7: Voltages and currents of the GFM inverter under different grid strengths.

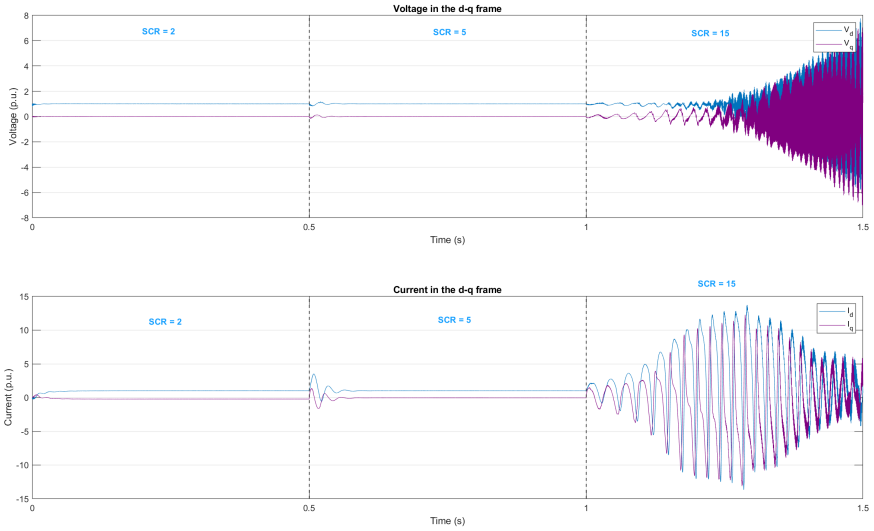

Figure 4.8: Voltages and currents in the d-q frame of the GFM inverter under different grid strengths.

and becomes unstable. This highlights the unique characteristic of GFM inverters, where high grid strength (high SCR) can induce instability.

4.5. Case 3: GFL in parallel with a GFM connected to the infinite grid

In this section, we will test the case where some capacity of GFM is installed in parallel with a GFL in order to increase the strength of the system. This setup has been widely implemented in industry and is aligned with many ongoing real-world GFM projects [9]. We assume the setup as shown in figure 4.9. We assume aggregated GFL generation connected to the HV through two step-up transformers. The GFM, which most of the time is a battery energy storage system, is also connected to the HV. The GFM, apart from increasing the system strength, it is also used to compensate for renewable energy fluctuations.

The objective is to determine the minimum capacity of the GFM required to ensure system stability. In this analysis, the GFM is represented by its voltage-source behaviour. As discussed in section 3.5, for small-signal studies, the GFM can be approximated as an infinite source in series with an impedance, whose magnitude depends on the chosen control strategy and parameter settings. This magnitude is evaluated through the largest singular value of the impedance model across the frequency spectrum. A key question, however, is which frequency is most relevant. Since the instabilities originate from the GFL, the focus should be on the frequency associated with its dominant poles, those that could lead to instability.

Consider first the single GFL connected to an infinite bus through the line impedance $Z_{\text{line}} = jX_{\text{line}}$. The short-circuit ratio (SCR) at the GFL bus is then defined as

$$\text{SCR}_0 = \frac{V_N^2}{S_{\text{GFL}}\,|X_{\text{line}}|} = \frac{V_N^2}{S_{\text{GFL}}}\,B_{\text{line}}, \tag{4.4}$$

where V_N is the nominal bus voltage, S_{GFL} the rated capacity of the GFL, and $B_{\text{line}} = 1/X_{\text{line}}$ the line susceptance.

When a GFM is added at the same bus, it is modelled in small-signal as an ideal voltage source in series with $Z_{\text{GFM}} = jX_{\text{GFM}}$. Since both sources are connected to the same infinite bus, the equivalent network as seen from the GFL bus is simply the parallel combination of the two paths as shown below:

$$B_{\text{eq}} = B_{\text{line}} + B_{\text{GFM}}, \qquad B_{\text{GFM}} = \frac{1}{X_{\text{GFM}}}. \tag{4.5}$$

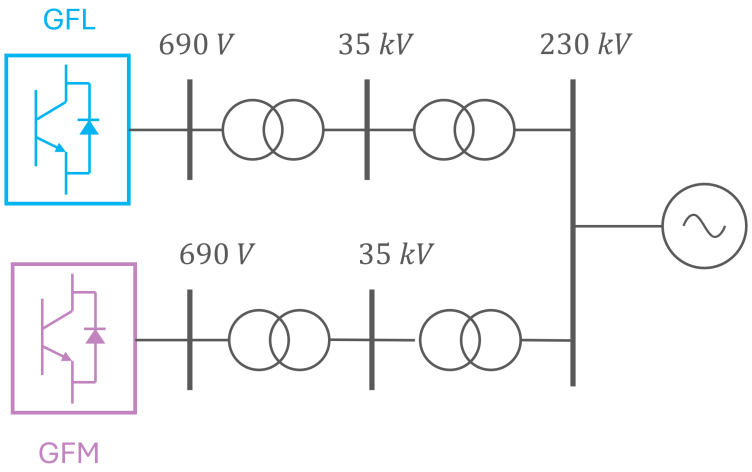

Figure 4.9: GFL inverter connected with a GFM in parallel to the HV.

The new SCR becomes

$$\mathrm{SCR} = \frac{V_N^2}{S_{\mathrm{GFL}}}\,(B_{\mathsf{line}} + B_{\mathsf{GFM}}) = \mathrm{SCR}_0 + \frac{V_N^2}{S_{\mathrm{GFL}}\,|X_{\mathsf{GFM}}|}. \tag{4.6}$$

Defining the capacity ratio as

$$\gamma = \frac{S_{\mathrm{GFM}}}{S_{\mathrm{GFL}}}, \tag{4.7}$$

and writing the GFM's own contribution in per-unit on its base as

$$Y_{\mathrm{GFM}}^{(\mathrm{pu})} = \frac{V_N^2}{S_{\mathrm{GFM}}\,|X_{\mathsf{GFM}}|}, \tag{4.8}$$

the expression can be compactly written as

$$\mathrm{SCR} = \mathrm{SCR}_0 + \gamma\, Y_{\mathrm{GFM}}^{(\mathrm{pu})} \tag{4.9}$$

This shows that the GFM increases the effective grid strength additively. That means that if the Ylocal can be calculated, then we can solve for γ to obtain the desired SCR. Below we have an example:

Suppose that the GFL inverter described in Case 1 is connected to an infinite bus through two step-up transformers. The grid is considered weak, with an SCR of 1.5 at the HV bus. Each transformer is assumed to have a reactance of 0.1 p.u. As shown in Case 1, the corresponding critical SCR (CSCR) is 2.3. This means that, in order to stabilise the system, additional GFM capacity must be introduced such that the effective SCR exceeds the CSCR. To determine the required capacity, we utilise the equation 4.10.

The first step is to calculate Y_{local}, which consists of the transformer reactance and the internal admittance of the GFM. To obtain this, we perform eigenvalue analysis of the GFL to identify the frequency of the unstable poles. As shown in figure 4.10a, the unstable poles at SCR=1.5 are located at 32 Hz. Next, we evaluate the singular values of the GFM impedance and determine its magnitude at this frequency. From figure 4.10b, the largest singular value is approximately -37 dB, corresponding to about 0.01 p.u.

By using equation 4.10 we calculate:

$$\gamma \geq (\mathrm{CSCR} - \mathrm{SCR}_0)(Z_{Tran} + Z_{GFM}) = 16.8\% \tag{4.10}$$

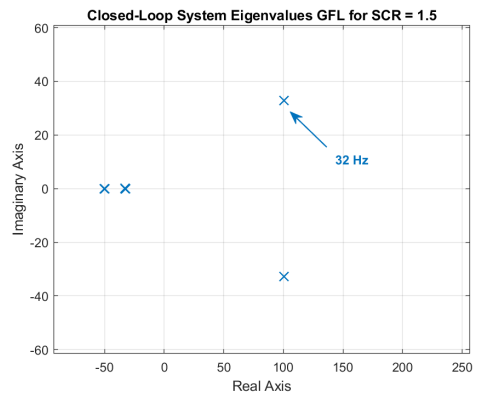

(a) Unstable poles of closed system of GFL inverter at SCR=1.5.

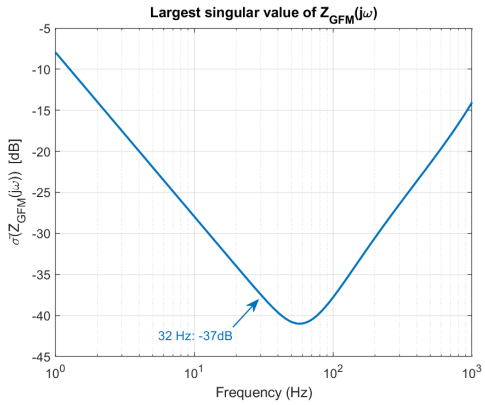

(b) Largest singular value of GFM inverter's impedance at 60 Hz.

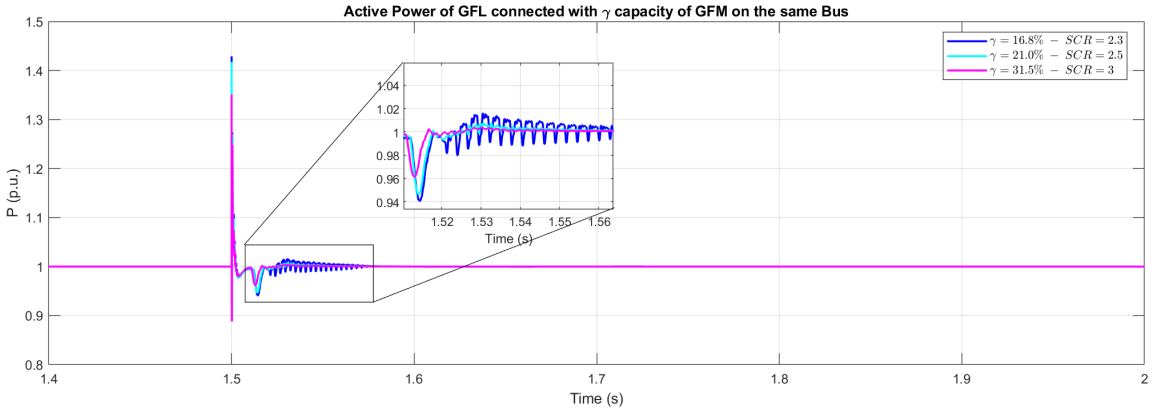

Figure 4.11: Response of the GFL inverter for different capacity ratios γ.

In figure 4.11, the active power responses of the GFL inverter to a 5% voltage sag at the 230 kV HV bus at $t = 1.5s$ are shown. Three different capacity ratios are tested. For $\gamma = 16.8\%$, the system exhibits oscillations for several seconds. When larger GFM capacities are used, the response becomes more damped. For values below the one calculated in equation 4.10, the system becomes unstable, as it cannot reach the required grid strength.

4.6. Case 4: Simulation of multiple grid-connected IBRs

In this section, the case of five identical GFL inverters connected to a test grid is examined. The network parameters are summarised in table 4.4. The Simulink implementation of the network can be found in Appendix A.

For this case, the parameters of the GFLs are in table 4.3. From the stability analysis of the single IBR, the CSRC was found to be around 2.1. In this case we assume that all GFLs have the same power ratings, i.e. $S_B = diag\{1, 1, 1, 1, 1\} = I_5$.

As an example, we assume the test network depicted in figure 4.12 as used in [11]. The network consists of five IBRs ($m = 5$), 2 internal nodes ($n = 2$) and three infinite buses ($k = 3$). The inductances of the transmission lines of the network are listed in figure 4.12. The rated capacities of the IBRs with respect to the global power base are $S_B = diag\{1, 2, 3, 1, 2\}$.

We assume that all the IBRs are the GFL inverters used in section 3.3. Based on the stability analysis conducted, the $CSCR = 2.85$ for the single IBR connected to the grid.

We calculate the matrix Y_{eq} by constructing the suspectance matrix for the whole network. After that, we delete the last 3 rows and columns, which represent the infinite buses which are grounded. After applying Kron reduction (equation 3.40) to the grounded Laplacian, we get:

Table 4.3: GFL inverter parameters for the multiple IBR network.

Symbol	Description	Value
f	Grid frequency	60 Hz
S_{base}	Base apparent power	1.5 MVA
V_{base}	Base line-to-line RMS voltage	690 V
V_{dc}	DC voltage	1,069 kV
L_f^{pu}	Filter inductance	0.05 p.u.
C_f^{pu}	Filter capacitance	0.06 p.u.
$K_{\text{CC},P}$	PI current controller proportional gain	314.16
$K_{\text{CC},I}$	PI current controller integral gain	493,488
$K_{\text{PLL},P}$	PLL proportional gain	62.83
$K_{\text{PLL},I}$	PLL integral gain	986.96
T_{VF}	Voltage feedforward filter time constant	0.01
K_{VF}	Voltage feedforward filter gain	1
P_{set}^{pu}	Active power setpoint	1 p.u.
Q_{set}^{pu}	Reactive power setpoint	0 p.u.

Table 4.4: Line inductances used in the test network in p.u.

L_{14}	0.1	L_{16}	0.2	L_{23}	0.2
L_{25}	0.1	L_{26}	0.1	L_{34}	0.15
L_{47}	0.16	L_{57}	0.08	L_{67}	0.3
L_{68}	0.1	L_{39}	0.05	$L_{7,10}$	0.2

$$Q_{\text{red}} = \begin{bmatrix} 14.10 & -1.79 & 0 & -10.14 & -0.28 \\ -1.79 & 21.42 & -5.00 & -0.28 & -10.55 \\ 0 & -5.00 & 31.67 & -6.67 & 0 \\ -10.14 & -0.28 & -6.67 & 21.45 & -2.93 \\ -0.28 & -10.55 & 0 & -2.93 & 16.65 \end{bmatrix}. \tag{4.11}$$

The eigenvalues of Y_{eq} are $\lambda_1 = 2.56, \lambda_2 = 7.29, \lambda_1 = 10.85, \lambda_1 = 15.12, \lambda_1 = 29.32$. The gSCR of the network is given as the smallest among the eigenvalues:

$$\text{gSCR} = \lambda_{\min}(S_B^{-1} Q_{red}) = \lambda_{\min}(Y_{eq}) = \lambda_1 = 2.56 \tag{4.12}$$

The stability criterion requires that $gSCR > CgSCR$ in order to ensure system stability. In this case, the calculated gSCR is lower than the CSCR of the GFL inverter, which indicates that the system does not meet the minimum strength needed to maintain stable operation. As a result, the system is predicted to be unstable under the given conditions without the need to conduct extensive eigenvalue analysis of the whole closed-loop system.

The same system is tested in time domain simulations. The simulation runs for 1 sec. For $t \leq 0.5s$ the network has the predefined line parameters and it is strong with $gSCR = \lambda_{min}(S_B^{-1} Q_{red}) = 4$. For $0.5s < t \leq 1s$, the lines connecting the three infinite buses to the rest of the network become weaker. More specifically, $L_{68} = 0.2$, $L_{39} = 0.3$ and $L_{7,10} = 0.3$. This change alters the gSCR, which is equal to $gSCR' = 1.93$. Based on the theoretical assessment, since the CSCR of the GFL is 2.1 it is expected that the system will become unstable after the $t = 0.5s$.

In figure 4.13, the voltage V_d of the single GFL inverter connected to an infinite grid is shown. In contrast, figure 4.14 presents the voltages V_{d1} to V_{d5} of the five GFL inverters connected to the test network. It is evident that as the grid becomes weaker, the system transitions to an unstable state, which confirms the theoretical analysis. Furthermore, it is worth noting that both figures show similar dynamic behaviour. This observation supports the interpretation that the overall system effectively behaves as a combination of five decoupled individual subsystems.

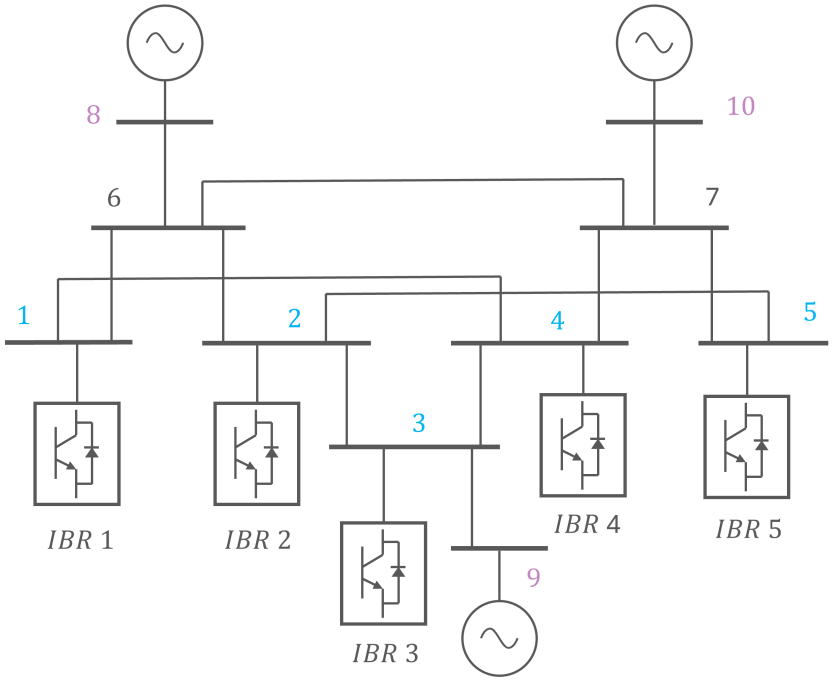

Figure 4.12: Test grid for the multiple IBR case.

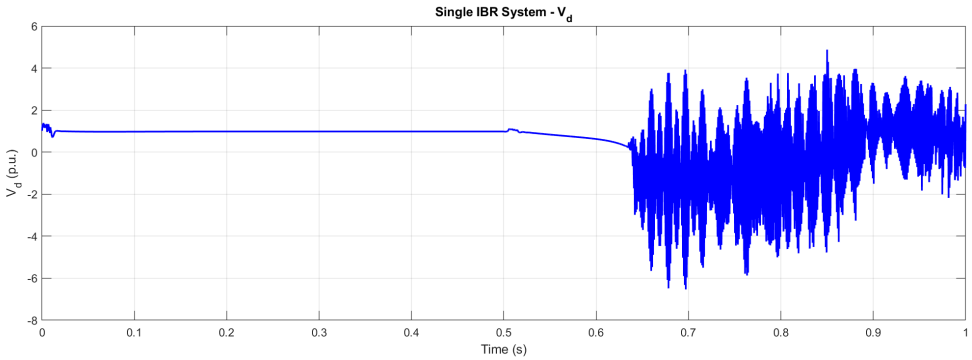

Figure 4.13: Voltage of the d-axis of the GFL in the single IBR system.

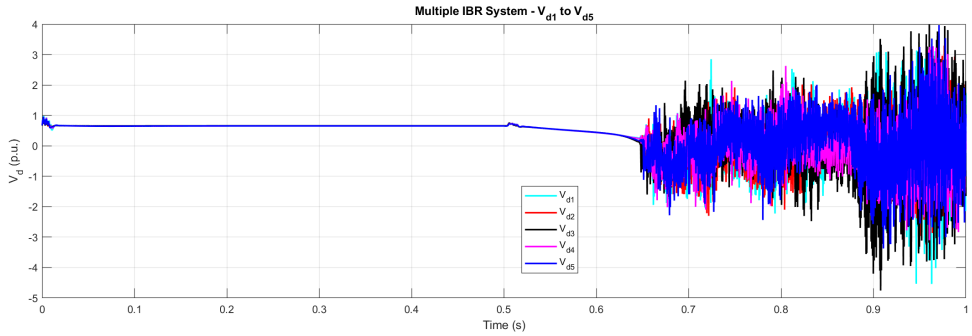

Figure 4.14: Voltage of the d-axis of the 5 GFLs in the multiple IBR system.

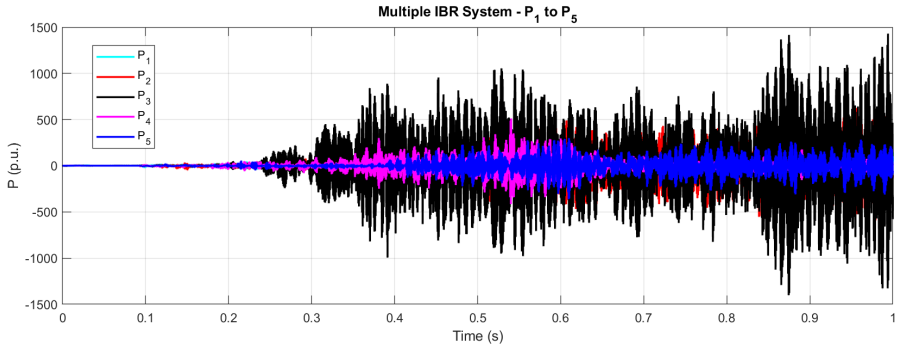

Figure 4.15: Graph of the active power of all generations. The system cannot stabilise if the GFM inverter is positioned on bus 3.

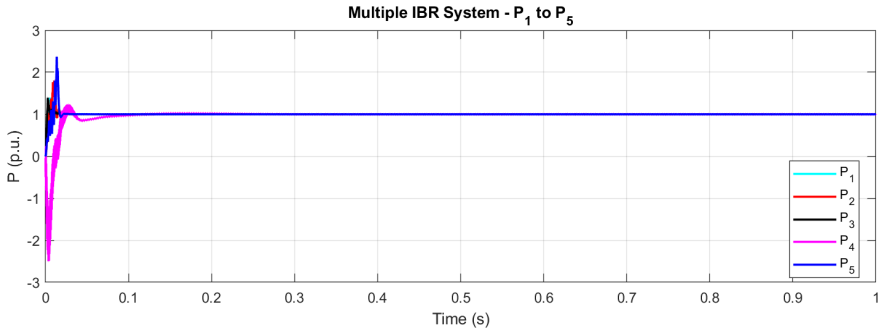

Figure 4.16: Graph of the active power of all generations. The system manages to stabilise when the GFM inverter is positioned on bus 4.

The next test, conducted on the same grid, assumes that the grid is already weak. We assume gSCR=1.6. The goal is to find a way to increase the strength of the system. One approach could be to replace one of the GFL inverters with a GFL. In order to do that, the idea of modelling the GFM as an ideal voltage source can be tested and checked if it sufficiently supports the desired system strength. Since the GFM is represented as an ideal voltage source, the bus where the GFM is going to be positioned can be grounded while creating the grounded Laplacian. So the strategy is to try all possible locations of the GFMs, calculate the Y_{eq} and finally the gSCR. The position that yields the largest gSCR is the best position.

Table 4.5: Calculated gSCR values for each bus

GFM Bus	New gSCR
1	2.7829
2	2.4050
3	2.0015
4	3.0062
5	2.4007

In table 4.5, the new gSCR are calculated for each bus where the GFM is installed. As shown, only bus 3 cannot yield the necessary strength, so it is not possible. For best results, the GFM should replace the GFM on bus 4.

Next, simulations were carried out by replacing the GFL inverters with a GFM inverter one at a time. As shown in figure 4.15, certain placements fail to stabilise the system, whereas in figure 4.16 the system remains stable when the optimal location is selected.

4.7. Discussion and design recommendations

As discussed in the previous section, the GFM is modelled as an ideal voltage source and can therefore be grounded within the gSCR framework. In the earlier example, however, the internal impedance of the GFM was not considered. In a large network, the dominant poles of each GFL depend on their location, making them difficult to identify. To investigate this further, the system was tested under reduced gSCR values in order to stress its stability limits. It was observed that for gSCR values below 2.6, the GFM became unstable, which represents a significant deviation from the CSCR of 2.1. For instance, when the GFM was placed at bus 5, instability occurred already for gSCR < 2.2. This indicates that the new stability boundaries are strongly dependent on the placement of the GFM.

One possible approach to address this issue is to make the GFM inverter with stronger ideal voltage source behaviour. The critical frequencies correspond to the PLL poles, which typically lie in the range of 1-200 Hz [9]. By adjusting the control parameters of the GFM, it was found that tuning the PI controller of the voltage loop can make the GFM behave as a stiffer voltage source. Furthermore, adding virtual damping in the swing equation provides additional stabilising effects.

However, it needs to be noted that the selected GFM control scheme selected is the one with the lowest singular values in comparison with the other control techniques. That was also shown in figure 3.7. So when selecting a GFM control, it is important to include the series impedance since this value could be significant and would give more precise results.

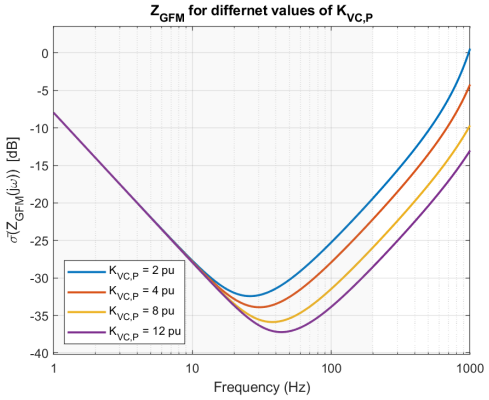

(a) Largest Singular values of the GFM impedance under VSM control without Q droop, for varying values of the proportional gain of the PI controller of the control loop.

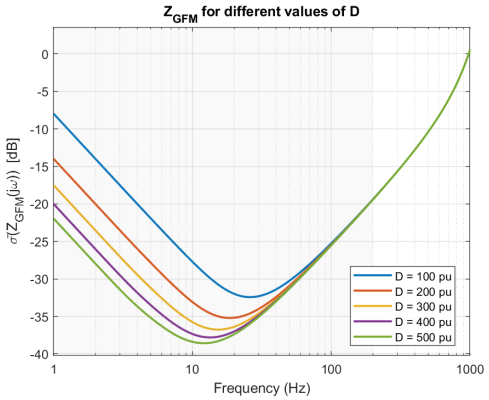

(b) Largest Singular values of the GFM impedance under VSM control without Q droop, for varying values of the virtual damping.

Another issue with the selected control schemes is the voltage drop observed under weak grid conditions. Recall that the GFL control includes both the PLL and the current control, with its references directly obtained from the power equation. The GFM control, in contrast, consists of voltage and current loops together with the VSM. Under weak grid conditions, GFL inverters experience voltage drops of about ± 5 p.u.. This occurs because, as the grid voltage decreases, the GFL is forced to maintain 1 p.u. of active power, which causes the currents to rise.

When a GFM is connected to a weak grid, even if it succeeds in stabilising the system, it becomes the only device providing voltage regulation and therefore injects large amounts of reactive power. An example of this behaviour can be seen in the test grid of Case 4. In figure 4.18, the voltages of all IBRs are shown when the gSCR is 4.5, while in figure 4.19 the case with gSCR = 7.5 is depicted. Although a gSCR of 4.5 may be considered a satisfactory level of system strength, the voltage drops are unacceptable, with the GFM injecting nearly 1 p.u. of reactive power. Thus, even though the system is stable, the injected currents are not acceptable.

In conclusion, while the gSCR framework provides a useful indication of suitable locations for GFMs, it does not account for component limits. A practical solution is either to install additional capacity beyond the minimum requirement or to install multiple GFMs so that more IBRs can contribute to voltage regulation. However, if a large GFM capacity is required to maintain acceptable current and voltage levels, the solution may prove financially unviable.

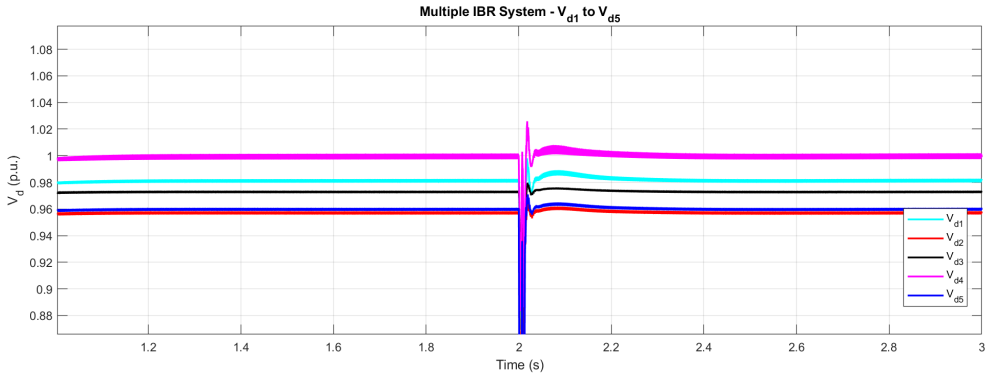

Figure 4.18: Voltages of the IBRs when gSCR = 4.5.

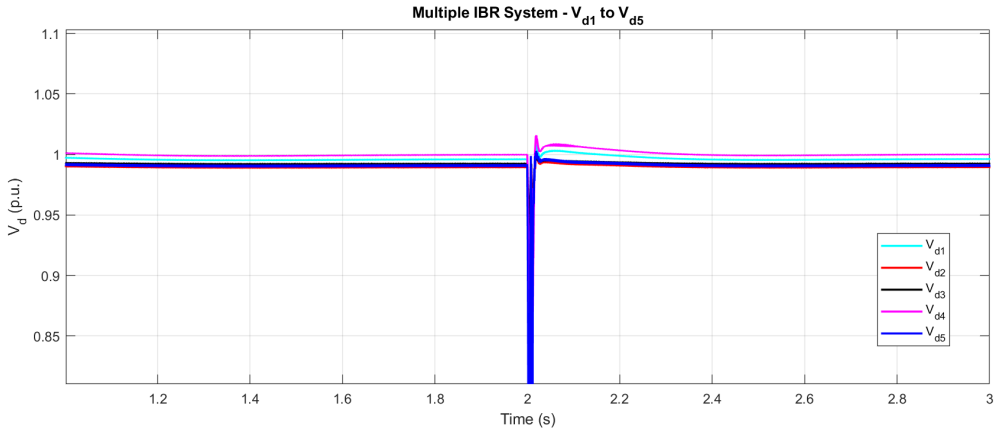

Figure 4.19: Voltages of the IBRs when gSCR = 7.5.

Another option is to adopt alternative GFM control strategies. For example, incorporating a Q-droop controller alongside other GFMs can enhance damping and improve power sharing, although this comes at the trade-off of reducing the effective strength that the GFM can provide to the system. In addition, a voltage loop can be integrated into the GFL control, as implemented in the work of Xin et al. [9].

5

Conclusion

This thesis investigated approaches to assess the stability boundaries in grids with high penetration of inverter-based resources (IBRs). The analysis combined impedance modelling, eigenvalue stability analysis, and the concepts of the short-circuit ratio (SCR) and generalized short-circuit ratio (gSCR). Based on this framework, the following research questions were addressed:

1. **What stability issues are posed by grid-following (GFL) inverters under weak grid conditions?**
   A single GFL inverter connected to an infinite bus was analysed. By combining impedance modelling of the control loops with the network, the closed-loop poles were studied across a range of SCR values. It was shown that under weak grid conditions, the poles cross into the right half-plane, defining the critical SCR (CSCR). This instability arises because the GFL relies on a PLL to track the grid voltage, which becomes unreliable in weak grids, leading to loss of synchronism. These findings were validated through time-domain simulations, confirming the link between PLL dynamics and weak-grid instability.
2. **What stability issues are posed by grid-forming (GFM) inverters under different grid conditions?**
   A single GFM inverter, modelled as a virtual synchronous machine without reactive power droop, was tested against an infinite bus. Eigenvalue analysis revealed that under strong grid conditions, instabilities can occur due to the interaction of two stiff voltage sources attempting to enforce their voltage profiles simultaneously. This highlights the duality: while GFLs are prone to weak-grid instability, GFMs can exhibit strong-grid instability, consistent with the duality theory of Li et al.
3. **What mathematical tools can determine the stability boundaries of GFL and GFM in single-inverter systems?**
   For both inverter types, small-signal stability analysis based on impedance models provides an effective tool to determine stability margins, even in black-box settings. The SCR framework is useful for single-inverter systems: the CSCR quantifies the stability boundary of a GFL, while for a GFM the internal impedance representation enables stability assessment. Singular value decomposition was employed to characterise the GFM impedance at the frequency of unstable GFL poles, enabling estimation of the minimum GFM penetration required to stabilise the system.
4. **What mathematical tools can determine the stability boundaries of IBRs in multi-inverter systems?**
   In multi-inverter grids, the gSCR generalises the SCR by accounting for network topology and converter interactions. Starting from the system admittance matrix, infinite buses were grounded and internal nodes eliminated via Kron reduction. The smallest eigenvalue of the reduced admittance matrix defines the gSCR, which acts as the equivalent grid strength. Stability is ensured if the gSCR exceeds the CSCR derived from the single-inverter case. Moreover, by modelling GFMs as voltage sources behind internal impedances, the framework also supports placement studies: checking all the possible locations and then determining the best location it can be placed.

In summary, this thesis demonstrated that:

- While GFL inverters are limited by PLL-induced weak grid instability, GFM inverters can face strong grid instabilities due to voltage-source interactions.
- Impedance-based small-signal analysis and SCR/gSCR frameworks can be useful mathematical tools to identify stability boundaries. By assuming that all the GFL controls share the same control parameters, a multi-IBR system can be decoupled into several single-IBR systems.
- By modelling GFMs as ideal voltage sources (in the small-signal sense) and combining this representation with the gSCR framework, a good starting indication of both the optimal placement of a GFM and the minimum capacity required is given.

Based on the above we can answer the main research question: ”**How can operators assess the stability boundaries of networks with high penetration of IBRs?**”

Overall, this thesis provides a useful guideline for grid operators when assessing potential changes in a network. The first step is to determine the critical SCR of a GFL inverter through small-signal stability analysis or simulations. This information can then be extended to multi-IBR systems, where the gSCR is calculated, and different scenarios regarding the placement and capacity of additional inverters can be evaluated. In addition, modelling GFMs as voltage sources behind an impedance offers further insight into the most suitable locations for their installation in order to increase the system strength.

5.1. Limitations and Future Work

This study has several limitations that call for further research. First, all grid-following inverters were assumed to have identical parameters. In practice, different manufacturers, control designs, and network conditions will result in heterogeneous behaviour, which makes the gSCR framework not applicable. Apart from that, the test grids were modelled with the same ratio R/X for the whole grid. Apart from that, all the cases tested were highly inductive networks.

Second, relatively simple models of both GFL and GFM inverters were employed. More advanced GFM control schemes can be introduced that may result in better response, such as power sharing, current limiting and overall stability. In addition, the implementation of current limiting in GFM inverters was only considered in a basic form. In reality, current-limiting strategies strongly influence both transient and small-signal behaviour, particularly under fault conditions or in weak grids. More advanced current-limiting mechanisms should therefore be included in future studies.

Third, the gSCR was used as the primary stability metric. However, gSCR evaluates system strength from the perspective of GFL inverters. A complementary tool is still lacking to characterise the system from the perspective of GFM inverters and voltage source interactions, to answer questions such as the maximum penetration of GFM capacity.

Finally, the analysis assumed that the DC side voltage is maintained constant and that there is sufficient DC-side energy storage capacity. However, in reality, the energy storage from the DC side can be limited and hence does not offer sufficient voltage source behaviour.

References

[1] IEA, *Wind - iea*, 2024. [Online]. Available: https://www.iea.org/energy-system/renewables/wind.

[2] IEA, *Solar*, 2024. [Online]. Available: https://www.iea.org/energy-system/renewables/solar-pv.

[3] Y. Li, Y. Gu, and T. C. Green, *Revisiting Grid-Forming and Grid-Following Inverters: A Duality Theory*, en, 2021. DOI: 10.48550/ARXIV.2105.13094. [Online]. Available: https://arxiv.org/abs/2105.13094.

[4] R. Aljarrah, B. B. Fawaz, Q. Salem, M. Karimi, H. Marzooghi, and R. Azizipanah-Abarghooee, "Issues and Challenges of Grid-Following Converters Interfacing Renewable Energy Sources in Low Inertia Systems: A Review," *IEEE Access*, vol. 12, pp. 5534–5561, 2024, ISSN: 2169-3536. DOI: 10.1109/ACCESS.2024.3349630. [Online]. Available: https://ieeexplore.ieee.org/document/10380571/.

[5] J. Matevosyan, B. Badrzadeh, T. Prevost, *et al.*, "Grid-Forming Inverters: Are They the Key for High Renewable Penetration?" *IEEE Power and Energy Magazine*, vol. 17, no. 6, pp. 89–98, 2019, ISSN: 1540-7977, 1558-4216. DOI: 10.1109/MPE.2019.2933072. [Online]. Available: https://ieeexplore.ieee.org/document/8879610/.

[6] P. Denholm, T. Mai, R. Kenyon, B. Kroposki, and M. O'Malley, "Inertia and the Power Grid: A Guide Without the Spin," Tech. Rep. NREL/TP-6A20-73856, 1659820, MainId:6231, 2020, NREL/TP–6A20–73 856, 1659820, MainId:6231. DOI: 10.2172/1659820. [Online]. Available: https://www.osti.gov/servlets/purl/1659820/.

[7] A. Boricic, J. L. R. Torres, and M. Popov, "System Strength: Classification, Evaluation Methods, and Emerging Challenges in IBR-dominated Grids," in *2022 IEEE PES Innovative Smart Grid Technologies - Asia (ISGT Asia)*, Singapore, Singapore: IEEE, 2022, pp. 185–189. DOI: 10.1109/isgtasia54193.2022.10003499. [Online]. Available: https://ieeexplore.ieee.org/document/10003499/.

[8] A. Boricic, J. L. R. Torres, and M. Popov, "System Strength: Classification, Evaluation Methods, and Emerging Challenges in IBR-dominated Grids," in *2022 IEEE PES Innovative Smart Grid Technologies - Asia (ISGT Asia)*, Singapore, Singapore: IEEE, 2022, pp. 185–189. DOI: 10.1109/isgtasia54193.2022.10003499. [Online]. Available: https://ieeexplore.ieee.org/document/10003499/.

[9] H. Xin, C. Liu, X. Chen, Y. Wang, E. Prieto-Araujo, and L. Huang, "How Many Grid-Forming Converters Do We Need? a Perspective From Small Signal Stability and Power Grid Strength," *IEEE Transactions on Power Systems*, pp. 1–13, 2024, ISSN: 0885-8950, 1558-0679. DOI: 10.1109/TPWRS.2024.3393877. [Online]. Available: https://ieeexplore.ieee.org/document/10508461/.

[10] V. Geekiyanage and J. Seppänen, "Power System Stability Improvements Through Grid Forming Inverters for Systems with High Penetration of Grid Following Inverters," in *2024 IEEE PES Innovative Smart Grid Technologies Europe (ISGT EUROPE)*, Dubrovnik, Croatia: IEEE, 2024, pp. 1–5, ISBN: 979-8-3503-9042-1. DOI: 10.1109/ISGTEUROPE62998.2024.10863434. [Online]. Available: https://ieeexplore.ieee.org/document/10863434/.

[11] W. Dong, H. Xin, D. Wu, and L. Huang, "Small Signal Stability Analysis of Multi-Infeed Power Electronic Systems Based on Grid Strength Assessment," *IEEE Transactions on Power Systems*, vol. 34, pp. 1393–1403, 2019, ISSN: 0885-8950, 1558-0679. DOI: 10.1109/TPWRS.2018.2875305. [Online]. Available: https://ieeexplore.ieee.org/document/8488538/.

[12] C. Henderson, A. Egea-Alvarez, and L. Xu, “Analysis of optimal grid-forming converter penetration in AC connected offshore wind farms,” *International Journal of Electrical Power & Energy Systems*, vol. 157, p. 109 851, 2024, ISSN: 01420615. DOI: 10.1016/j.ijepes.2024.109851. [Online]. Available: https://linkinghub.elsevier.com/retrieve/pii/S0142061524000723.

[13] S. Li, H. Wang, Y. Huang, G. He, C. Liu, and W. Wang, “Dynamic Interaction and Stability Analysis of Grid-following Converter Integrated Into Weak Grid,” *CSEE Journal of Power and Energy Systems*, 2025, ISSN: 20960042. DOI: 10.17775/CSEEJPES.2024.04920. [Online]. Available: https://ieeexplore.ieee.org/document/10838264.

[14] X. Ji, D. Liu, K. Jiang, Z. Zhang, and Y. Yang, “Small-Signal Stability of Hybrid Inverters with Grid-Following and Grid-Forming Controls,” *Energies*, vol. 17, p. 1644, 2024, ISSN: 1996-1073. DOI: 10.3390/en17071644. [Online]. Available: https://www.mdpi.com/1996-1073/17/7/1644.

[15] X. Gao, D. Zhou, A. Anvari-Moghaddam, and F. Blaabjerg, “Stability Analysis of Grid-Following and Grid-Forming Converters Based on State-Space Modelling,” *IEEE Transactions on Industry Applications*, vol. 60, no. 3, pp. 4910–4920, 2024, ISSN: 0093-9994, 1939-9367. DOI: 10.1109/TIA.2024.3353158. [Online]. Available: https://ieeexplore.ieee.org/document/10398460/.

[16] “Definition and Classification of Power System Stability IEEE/CIGRE Joint Task Force on Stability Terms and Definitions,” en, *IEEE Transactions on Power Systems*, vol. 19, no. 3, pp. 1387–1401, Aug. 2004, ISSN: 0885-8950. DOI: 10.1109/TPWRS.2004.825981. [Online]. Available: http://ieeexplore.ieee.org/document/1318675/.

[17] N. Hatziargyriou, J. Milanovic, C. Rahmann, *et al.*, “Definition and Classification of Power System Stability – Revisited & Extended,” en, *IEEE Transactions on Power Systems*, vol. 36, no. 4, pp. 3271–3281, Jul. 2021, ISSN: 0885-8950, 1558-0679. DOI: 10.1109/TPWRS.2020.3041774. [Online]. Available: https://ieeexplore.ieee.org/document/9286772/.

[18] Y. Gu and T. C. Green, “Power System Stability With a High Penetration of Inverter-Based Resources,” en, *Proceedings of the IEEE*, vol. 111, no. 7, pp. 832–853, Jul. 2023, ISSN: 0018-9219, 1558-2256. DOI: 10.1109/JPROC.2022.3179826. [Online]. Available: https://ieeexplore.ieee.org/document/9796617/.

[19] IEEE, “IEEE Guide for Planning DC Links Terminating at AC Locations Having Low Short-Circuit Capacities,” *IEEE Std 1204-1997*, pp. 1–216, Jan. 1997, Conference Name: IEEE Std 1204-1997. DOI: 10.1109/IEEESTD.1997.85949. [Online]. Available: https://ieeexplore.ieee.org/document/653230/?arnumber=653230.

[20] P. Rodriguez and N. Lai, “Grid-following and grid-forming PV and wind turbines,” in *Control of Power Electronic Converters and Systems*, Elsevier, 2021, pp. 499–521, ISBN: 978-0-12-819432-4. DOI: 10.1016/B978-0-12-819432-4.00022-6. [Online]. Available: https://linkinghub.elsevier.com/retrieve/pii/B9780128194324000226.

[21] L. Ramirez, P. Bauer, and S. Izadkhast, *DC and AC Microgrids*, 1st ed. Delft, Netherlands, 2018.

[22] E. Ebinyu, O. Abdel-Rahim, D.-E. A. Mansour, M. Shoyama, and S. M. Abdelkader, “Grid-Forming Control: Advancements towards 100% Inverter-Based Grids—A Review,” *Energies*, vol. 16, no. 22, p. 7579, Nov. 2023, ISSN: 1996-1073. DOI: 10.3390/en16227579. [Online]. Available: https://www.mdpi.com/1996-1073/16/22/7579.

[23] Mathworks, *Park Transform - Implement abc to dq0 transform - Simulink*, en. [Online]. Available: https://nl.mathworks.com/help/sps/ref/parktransform.html.

[24] X. Wang, M. G. Taul, H. Wu, Y. Liao, F. Blaabjerg, and L. Harnefors, “Grid-Synchronization Stability of Converter-Based Resources—An Overview,” en, *IEEE Open Journal of Industry Applications*, vol. 1, pp. 115–134, 2020, ISSN: 2644-1241. DOI: 10.1109/OJIA.2020.3020392. [Online]. Available: https://ieeexplore.ieee.org/document/9181463/.

[25] L. Zhang, L. Harnefors, and H.-P. Nee, “Power-Synchronization Control of Grid-Connected Voltage-Source Converters,” en, *IEEE Transactions on Power Systems*, vol. 25, no. 2, pp. 809–820, May 2010, ISSN: 0885-8950, 1558-0679. DOI: 10.1109/TPWRS.2009.2032231. [Online]. Available: http://ieeexplore.ieee.org/document/5308285/ (visited on 02/17/2025).

[26] T. Jouini, C. Arghir, and F. Dörfler, "Grid-Friendly Matching of Synchronous Machines by Tapping into the DC Storage**This research is supported by ETH funds and the SNF Assistant Professor Energy Grant #160573.," en, *IFAC-PapersOnLine*, vol. 49, no. 22, pp. 192–197, 2016, ISSN: 24058963. DOI: 10.1016/j.ifacol.2016.10.395. [Online]. Available: https://linkinghub.elsevier.com/retrieve/pii/S2405896316319826.

[27] B. B. Johnson, M. Sinha, N. G. Ainsworth, F. Dorfler, and S. V. Dhople, "Synthesizing Virtual Oscillators to Control Islanded Inverters," en, *IEEE Transactions on Power Electronics*, vol. 31, no. 8, pp. 6002–6015, Aug. 2016, ISSN: 0885-8993, 1941-0107. DOI: 10.1109/TPEL.2015.2497217. [Online]. Available: http://ieeexplore.ieee.org/document/7317584/ (visited on 02/24/2025).

[28] G.-S. Seo, M. Colombino, I. Subotic, B. Johnson, D. Gros, and F. Dorfler, "Dispatchable Virtual Oscillator Control for Decentralized Inverter-dominated Power Systems: Analysis and Experiments," en, in *2019 IEEE Applied Power Electronics Conference and Exposition (APEC)*, Anaheim, CA, USA: IEEE, Mar. 2019, pp. 561–566, ISBN: 978-1-5386-8330-9. DOI: 10.1109/APEC.2019.8722028. [Online]. Available: https://ieeexplore.ieee.org/document/8722028/ (visited on 02/24/2025).

[29] Y. Liu, R. Huang, W. Du, A. Singhal, and Z. Huang, "Highly-Scalable Transmission and Distribution Dynamic Co-Simulation With 10,000+ Grid-Following and Grid-Forming Inverters," *IEEE Transactions on Power Delivery*, vol. 39, no. 1, pp. 578–590, Oct. 2024, ISSN: 1937-4208. DOI: 10.1109/TPWRD.2023.3302303. [Online]. Available: https://ieeexplore.ieee.org/document/10210125.

[30] C. Yang, L. Huang, H. Xin, and P. Ju, "Placing Grid-Forming Converters to Enhance Small Signal Stability of PLL-Integrated Power Systems," *IEEE Transactions on Power Systems*, vol. 36, no. 4, Jul. 2021, ISSN: 0885-8950, 1558-0679. DOI: 10.1109/TPWRS.2020.3042741. [Online]. Available: https://ieeexplore.ieee.org/document/9282199/.

[31] Y. Liu, Y. Chen, H. Xin, *et al.*, "System Strength Constrained Grid-Forming Energy Storage Planning in Renewable Power Systems," en, *IEEE Transactions on Sustainable Energy*, vol. 16, no. 2, pp. 981–994, Apr. 2025, ISSN: 1949-3029, 1949-3037. DOI: 10.1109/TSTE.2024.3494259. [Online]. Available: https://ieeexplore.ieee.org/document/10747388/.

[32] L. Huang, C. Wu, D. Zhou, and F. Blaabjerg, "Comparison of Three Small-Signal Stability Analysis Methods for Grid-Following Inverter," en, in *2021 International Aegean Conference on Electrical Machines and Power Electronics (ACEMP) & 2021 International Conference on Optimization of Electrical and Electronic Equipment (OPTIM)*, Brasov, Romania: IEEE, Sep. 2021, pp. 34–41, ISBN: 978-1-6654-0298-9. DOI: 10.1109/OPTIM-ACEMP50812.2021.9590036. [Online]. Available: https://ieeexplore.ieee.org/document/9590036/.

[33] L. Liyanarachchi, N. Hosseinzadeh, A. Gargoom, and E. M. Farahani, "A new index for the assessment of power system strength considering reactive power injection and interaction of inverter based resources," en, *Sustainable Energy Technologies and Assessments*, vol. 60, p. 103 460, Dec. 2023, ISSN: 22131388. DOI: 10.1016/j.seta.2023.103460. [Online]. Available: https://linkinghub.elsevier.com/retrieve/pii/S2213138823004538.

[34] C. Liu, H. Xin, D. Wu, and Y. Zhou, *Generalized Operational Short-Circuit Ratio for Grid Strength Assessment in Renewable Power Systems under Non-Rated Operating Conditions*, en, Aug. 2022. DOI: 10.36227/techrxiv.20692483.v1. [Online]. Available: https://www.techrxiv.org/doi/full/10.36227/techrxiv.20692483.v1.

[35] *1.7: Linearization of Nonlinear Models*, 2020. [Online]. Available: https://eng.libretexts.org/Bookshelves/Industrial_and_Systems_Engineering/Introduction_to_Control_Systems_(Iqbal)/01%3A_Mathematical_Models_of_Physical_Systems/1.07%3A_Linearization_of_Nonlinear_Models.

[36] L. Huang, H. Xin, W. Dong, and F. Dörfler, *Impacts of Grid Structure on PLL-Synchronization Stability of Converter-Integrated Power Systems*, arXiv:1903.05489 [cs], Nov. 2019. DOI: 10.48550/arXiv.1903.05489. [Online]. Available: http://arxiv.org/abs/1903.05489.

[37] A. Amirkhani and A. H. Barshooi, “Consensus in multi-agent systems: A review,” *Artificial Intelligence Review*, vol. 55, no. 5, pp. 3897–3935, Jun. 2022, ISSN: 1573-7462. DOI: 10.1007/s10462-021-10097-x. [Online]. Available: https://doi.org/10.1007/s10462-021-10097-x.

[38] X. Ru and W. Xia, “Spectral Properties of Grounded Laplacian Matrices for Multiplex Networks*,” en, *IFAC-PapersOnLine*, vol. 56, no. 2, pp. 7408–7413, 2023, Publisher: Elsevier BV, ISSN: 2405-8963. DOI: 10.1016/j.ifacol.2023.10.618. [Online]. Available: https://linkinghub.elsevier.com/retrieve/pii/S2405896323009898.

[39] F. Dorfler and F. Bullo, “Kron Reduction of Graphs With Applications to Electrical Networks,” *IEEE Transactions on Circuits and Systems I: Regular Papers*, vol. 60, no. 1, pp. 150–163, Jan. 2013, Publisher: Institute of Electrical and Electronics Engineers (IEEE), ISSN: 1549-8328, 1558-0806. DOI: 10.1109/tcsi.2012.2215780. [Online]. Available: http://ieeexplore.ieee.org/document/6316101/.

[40] C. Li, S. Wang, and J. Liang, “Tuning Method of a Grid-Following Converter for the Extremely-Weak-Grid Connection,” en, *IEEE Transactions on Power Systems*, vol. 37, no. 4, pp. 3169–3172, Jul. 2022, ISSN: 0885-8950, 1558-0679. DOI: 10.1109/TPWRS.2022.3167899. [Online]. Available: https://ieeexplore.ieee.org/document/9760224/.

[41] Y. Li, *Future-Power-Networks/Publications*, original-date: 2021-03-06T10:01:18Z, Aug. 2025. [Online]. Available: https://github.com/Future-Power-Networks/Publications.

A

Simulink Models

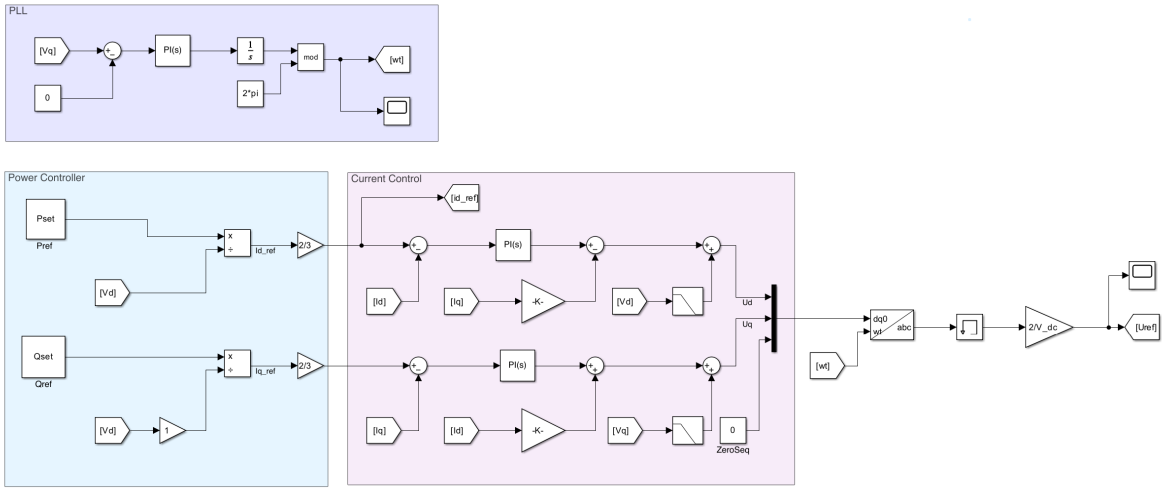

Figure A.1: Control diagram of the GFL control in Simulink.

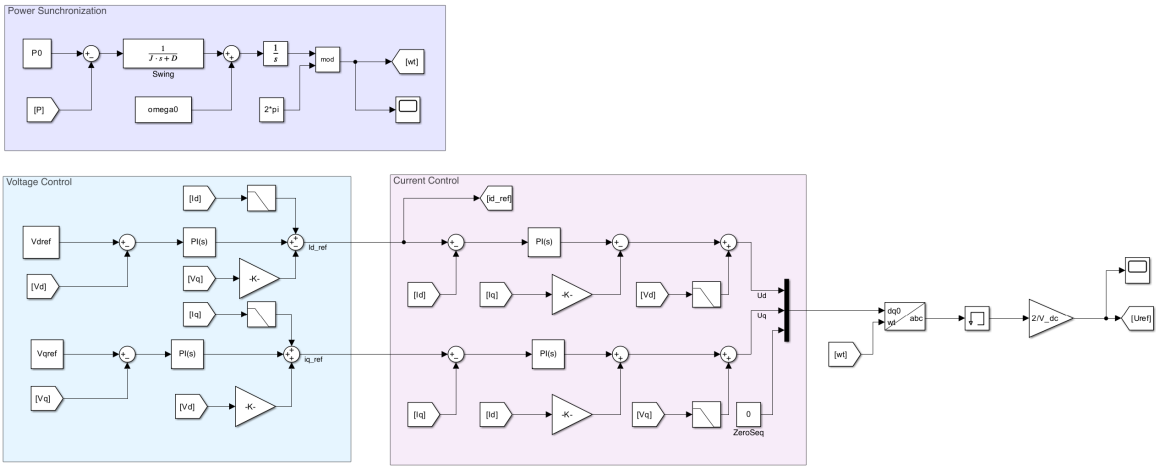

Figure A.2: Control diagram of the GFM control in Simulink.

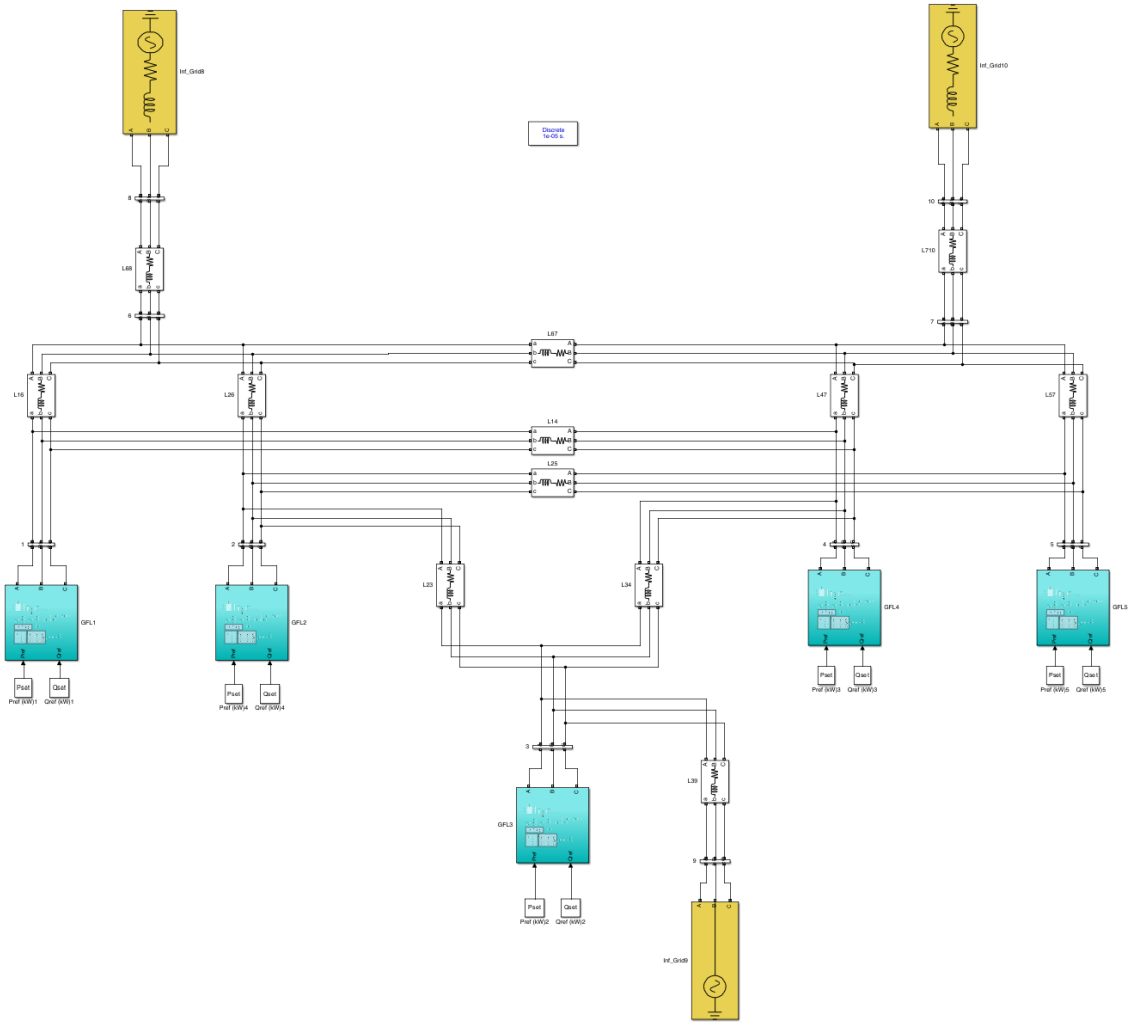

Figure A.3: Diagram of the test network with five GFL inverters in Simulink.

B

Admittance Models of GFL and GFM

Listing B.1: GFL Admittance Model

```
% Steady state (global dq, q=0)
ud0 = V_base*sqrt(2/3);                 % Vd0 (phase-peak)

% Use P = 1.5*Vd0*Id0 and Q = -1.5*Vd0*Iq0 →   Id0, Iq0:
Id0 = GFL.Pset/(1.5*ud0);
Iq0 = -GFL.Qset/(1.5*ud0);

%  Inner current loop + voltage feedforward
PI    = GFL.K_CC_P + GFL.K_CC_I/s;      % PI of current control
f_VF = K_VF/(T_VF*s + 1);               % voltage feedforward filter (0..1)

G_I   = PI/(s*GFL.L1 + PI);             % inner loop tracking factor
Y_VF = (1 - f_VF)/(s*GFL.L1 + PI);      % voltage feedforward path admittance

% 'Xins simplifications
% G_I  = 1;
% Y_VF = 0;

% Local (controller-frame) 2×2 admittance
% From i_d,ref =  P/(1.5*Vd), i_q,ref = -Q/(1.5*Vd):
%    i_d,ref /Vd =  -P/(1.5*Vd^2) = -Id0/Vd0
%    i_q,ref /Vd =  -Q/(1.5*Vd^2) =  +Iq0/Vd0   (since Iq0 = -Q/(1.5*Vd0))

Y_11 = Y_VF - G_I*(Id0/ud0);            % = Y_VF + G_I*P/(1.5*Vd0^2)
Y_12 = 0;
Y_21 = + G_I*(Iq0/ud0);                   % = -G_I*Q/(1.5*Vd0^2)
Y_22 = Y_VF;

% PLL mapping to global dq (q-axis measured)
PI_PLL   = K_PLL_P + K_PLL_I/s;
% Y_12_PLL = (s*Y_12 + PI_PLL*Iq0)/(s + PI_PLL*ud0);
Y_12_PLL = 0;
Y_22_PLL = (s*Y_22 - PI_PLL*Id0)/(s + PI_PLL*ud0);

Y_cl = [ Y_11      Y_12_PLL ;
         Y_21      Y_22_PLL ];

Y_cl = Y_cl;

% Add filter capacitor (at PCC)
Y_C = [ s*GFL.Cf   -omega*GFL.Cf ;
        omega*GFL.Cf  s*GFL.Cf   ];

Y_GFL = Y_cl + Y_C;
```

Listing B.2: GFM Addmitance Model

```

```

```
% Steady-state operating point in SI
Vd0 = V_base*sqrt(2/3);
P0  = S_base;
Q0  = 0;
Id0 = P0/(1.5*Vd0);
Iq0 = -Q0/(1.5*Vd0);

% --- Current loop  ---
PICC = K_CC_P + K_CC_I/s;
GI   = PICC / (s*Lf + PICC);
fVF  = K_VF / (T_VF*s + 1);
YVF  = (1 - fVF) / (s*Lf + PICC);

% --- Voltage PI ---
PIVC = K_VC_P + K_VC_I/s;

% --- Capacitor admittance in global dq  ---
YCL = [ s*Cf,  -omega0*Cf;
            omega0*Cf,  s*Cf ];

% --- Y0(s) ---
Y0  = (YVF + GI*PIVC + GI*(s*Cf)) / (1 - GI);

% --- Swing channel ---
Ysw = (Id0^2 - (Y0^2)*(Vd0^2)) / (J*s^2 + D*s);

% --- Total Y_GFM (eq. (5)) ---
YGFM = YCL + [ Y0, 0;
                   Ysw, Y0 ];
```